

Dark Matter Working Group recommendation for Two Higgs Doublet Model (draft title)

Authorlist to be compiled; Antonio Boveia,^{3,*} Caterina Doglioni,^{8,*} Kristian Hahn,^{14,*} Ulrich Haisch,^{15,16,*} Steven Lowette,²² Tim M.P. Tait,^{25,*}

*DMWG organizers

³Ohio State University, 191 W. Woodruff Avenue Columbus, OH 43210

⁸Fysiska institutionen, Lunds universitet, Lund, Sweden

¹⁴Department of Physics and Astronomy, Northwestern University, Evanston, Illinois 60208, USA

¹⁵Rudolf Peierls Centre for Theoretical Physics, University of Oxford, Oxford, OX1 3PN, United Kingdom

¹⁶CERN, TH Department, CH-1211 Geneva 23, Switzerland

²²Physics Department, Vrije Universiteit Brussel, Brussels, Belgium

²⁵Department of Physics and Astronomy, University of California, Irvine, California 92697, USA

Editor's E-mail: antonio.boveia@cern.ch, caterina.doglioni@cern.ch,
kristian.hahn@cern.ch, ulrich.haisch@physics.ox.ac.uk, ttait@uci.edu

Abstract. Draft abstract.

Contents

1	Introduction	1
2	The model	1
3	Model parameters	2
4	Parameter grid	4
4.1	Parameter scans on masses, couplings and mixing angles	4
4.1.1	Results of studies	4
4.1.2	Studies of the $h(bb) + E_T^{\text{miss}}$ signature	5
4.1.3	Studies of the mono-Z (leptonic) signature	17
4.1.4	Studies of DM+heavy flavor signature	27
4.1.5	Recasting existing $t\bar{t} + E_T^{\text{miss}}$ and $b\bar{b} + E_T^{\text{miss}}$ signatures	27
4.1.6	Motivation for a dedicated $tW + E_T^{\text{miss}}$ search	30
4.1.7	Uncovered signatures with $t\bar{t}h + E_T^{\text{miss}}$	30
4.1.8	Top pair resonant searches	31
4.1.9	Four tops final states	31
4.1.10	Final proposal for parameter scan	31
5	Connection with cosmology	33
5.1	TODO	33
5.2	Actual content	33
6	Conclusions	34

1 Introduction

Reasoning behind this effort

- Simplified models only one signature at a time, sometimes not gauge invariant
- One step beyond this: less-simplified models
- Compare and confront different search sensitivity
- Combinations among different signatures
- Find new kinematic regimes / improve searches by exploring different signatures
- Still keeping the choice of model generic enough that this is reusable for theorists

Reasoning behind this effort

- Reasoning behind the choice of model
- Highlights more than one signature at a time, depending on parameters
- Leaves room for new unexplored kinematic signatures within existing searches (left for future work)
- Complete enough, still simplified so that one can choose grid planes
- Existing theory effort (HXS WG)

2 The model

Description of the model

- Citations: [? ? ? ? ?]
- Particles, masses, couplings, mixing angles

Comparison with existing models How does the model compare with other 2HDMs/scalar models (with and without DM).

- Scalar to SSM to 2HDM evolution
- Other models:
 - S. Ipek, D. McKeen, A. Nelson, [?]
 - Bell, Busoni, Sanderson, [?]
 - No, Goncalves, Machado, [? ?]
 - Higgs Cross-section Working Group

3 Model parameters

- Motivate the choice of parameters in [?]
- Vacuum stability study: fix lambda parameters to 3

For extension of the Higgs sector (and in general for scalar extensions of the Standard Model) one needs to worry about boundedness from below of the scalar potential, as well as absolute stability of the electroweak minimum¹.

¹We remark here that implications from all indirect constraints - be it flavour, electroweak precision constraints or stability requirements - should be treated as preferred parameter space in a simplified model framework. It would contradict the idea of simplified models were these constraints taken at face value.

Regarding boundedness from below of the scalar potential in the present 2HDM + S model, we stress that provided that $\lambda_{P1}, \lambda_{P2} > 0$ in

$$V_P = \frac{1}{2}m_P^2 P^2 + \kappa (i P H_1^\dagger H_2 + \text{h.c.}) + \lambda_{P1} P^2 |H_1|^2 + \lambda_{P2} P^2 |H_2|^2,$$

the study of boundedness from below at tree-level reduces to the corresponding study in the 2HDM. The boundedness from below conditions in this case are well-known [?]:

$$\lambda_1 > 0, \lambda_2 > 0, \lambda_3 > -\sqrt{\lambda_1 \lambda_2}, \lambda_3 + \lambda_4 - |\lambda_5| > -\sqrt{\lambda_1 \lambda_2} \quad (3.1)$$

and can be inferred from analyzing the scalar potential at large field values $H_1, H_2 \gg v$. For $m_{H^\pm} = m_{H_0}$, the first two conditions in (3.1) may be simply written as

$$\frac{m_h^2}{v^2}(1 - t_\beta^2) + \lambda_3 t_\beta^2 > 0, \quad \frac{m_h^2}{v^2}(1 - t_\beta^{-2}) + \lambda_3 t_\beta^{-2} > 0 \quad (3.2)$$

which result in the requirement $\lambda_3 > m_h^2/v^2 = 0.258$. In figure 1 we show the regions of parameter space in the (m_a, m_{H_0}) (left) and (s_θ, m_a) (right) planes for which the tree-level boundedness from below conditions 3.1 are satisfied, assuming $m_{H^\pm} = m_{H_0} = m_{A_0}$.

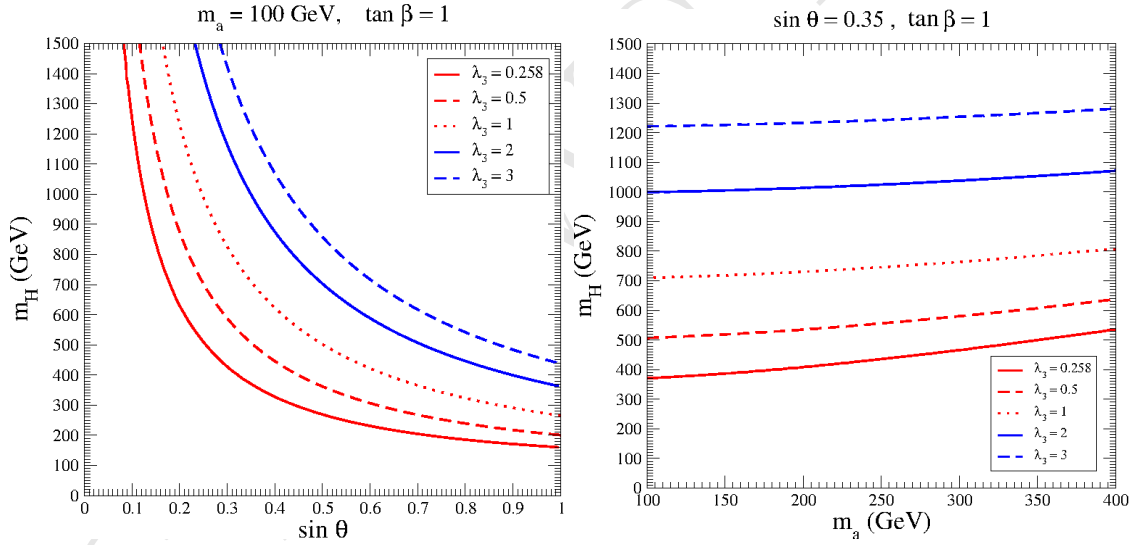


Figure 1: Regions of parameter space in the (m_a, m_{H_0}) (left) and (s_θ, m_a) (right) planes for which the tree-level boundedness from below conditions 3.1 are satisfied, assuming $m_{H^\pm} = m_{H_0} = m_{A_0}$.

Figure 1 shows that the region satisfying the tree-level boundedness from below conditions increases as λ_3 increases. At the same time, the choice $\lambda_3 = \lambda_{P1} = \lambda_{P2}$ which we adopt in the present analysis allows the increase in λ_3 not to affect the mono-Higgs sensitivity via a change in the coupling g_{aAh}

$$\begin{aligned} g_{aAh} &= \frac{c_\theta s_\theta}{m_H v} [m_h^2 + m_H^2 - m_a^2 - 2(\lambda_3 - \lambda_{P1} c_\beta^2 - \lambda_{P2} s_\beta^2) v^2] \\ &= \frac{c_\theta s_\theta}{m_H v} [m_h^2 + m_H^2 - m_a^2] \end{aligned} \quad (3.3)$$

We then fix the value $\lambda_3 = 3$ as benchmark for the rest of our analysis.

A few comments are in order.

- The choice of λ_3 , motivated by boundedness from below conditions, while not affecting the mono-Higgs sensitivity if $\lambda_3 = \lambda_{P1} = \lambda_{P2}$, has an impact on the mono- Z sensitivity since the coupling

$$\begin{aligned} g_{Haa} &= \frac{1}{m_H v} \left[2 t_{2\beta}^{-1} s_\theta^2 (m_h^2 - \lambda_3 v^2) + s_{2\beta} c_\theta^2 v^2 (\lambda_{P1} - \lambda_{P2}) \right] \\ &= \frac{1}{m_H v} \left[2 t_{2\beta}^{-1} s_\theta^2 (m_h^2 - \lambda_3 v^2) \right] \end{aligned} \quad (3.4)$$

does depend on λ_3 and influences the balance between $\Gamma(H_0 \rightarrow aa)$ and $\Gamma(H_0 \rightarrow Za)$ which ultimately determines the $H_0 \rightarrow Za$ branching fraction. In short, the choice of λ_3 , λ_{P1} , λ_{P2} affects either mono-Higgs or mono- Z sensitivities (or both).

- Together with boundedness from below, other potential constraints are usually considered in the context of the 2HDM and apply in general, among them unitarity (see e.g. [? ?]) and absolute stability of the electroweak vacuum (see e.g. [?]). In the present context we find these constraints are generically weaker than the boundedness from below condition and therefore disregard them in the following.
- The boundedness from below conditions are here evaluated at tree-level, but in a fully consistent treatment they should be evaluated including the effect of radiative corrections. This is however a much more involved process than what has been discussed above for the tree-level case (see e.g. [?]). In addition, the boundedness from below constraints discussed here are potentially sensitive to the existence of UV physics which our 2HDM+S simplified does not capture, and which could modify the above picture through the presence of higher-dimensional operators. Still, it is worth pointing out that for the 2HDM+S simplified model to be a good description of LHC phenomenology we require the new physics scale suppressing these effective operators to be above the TeV scale (since in our scans we are considering scalar masses up to ~ 1 TeV), and thus the presence of these high-energy operators is not expected to be of much help in case a runaway field direction exist at tree level in the 2HDM scalar potential.

4 Parameter grid

4.1 Parameter scans on masses, couplings and mixing angles

Logic of how we proceeded

- Starting from benchmark 3 of [?]

- Mapping the kinematics and sensitivity of the model by scanning some of the various parameters
- Checking whether other existing models can be rescaled

4.1.1 Results of studies

Each of the signatures should have the following plots in the planes of the final recommendation:

- efficiency at parton level with simplified, published cuts
- total and fiducial cross-section at parton level
- 2 - 3 kinematic plots of what has been scanned that are most representative for the analysis (here the analysers decide, then we harmonize at the end)

Signatures:

- Mono-Z (lep/had)
- MonoH \rightarrow bb
- Monojet
- ttbar+MET, with specific discussion about rescaling
- other signatures who have not yet presented at public meetings, in ATLAS and CMS

4.1.2 Studies of the $h(bb) + E_T^{\text{miss}}$ signature

The studies of the $h(bb) + E_T^{\text{miss}}$ channel presented here are based on Monte Carlo simulations with version 2.4.3 of MadGraph 5 [?] using a Universal FeynRules Output [?] implementation of the 2HDM with Dark Matter mediator with a Yukawa sector of type II provided by the authors of [?]. The PDF set used for these simulations is the NNPDF collaboration's NNPDF30_lo_as_0130 PDF set, a leading order five-flavor (assuming massless b -quarks) PDF set with $\alpha_S(m_Z) = 0.130$ [?]. For the matrix element calculation in MG5, the five-flavor scheme is chosen, and the b -quark mass set to zero.

The matrix element generated for the parton-level studies is $gg \rightarrow h\chi\bar{\chi}$. For the $M_a - \tan\beta$ scan (Figure 7, Figure 11), the matrix element $b\bar{b} \rightarrow h\chi\bar{\chi}$ is also generated. The additional matrix element is generated because at high $\tan\beta$ and for a Yukawa sector of type II, the $b\bar{b}$ initiated process can have an amplitude as large as, or even larger than, the gluon fusion initiated process [?]. However, gluon fusion dominates the remaining parameter space, so for all other scans the $b\bar{b}$ initiated process is neglected.

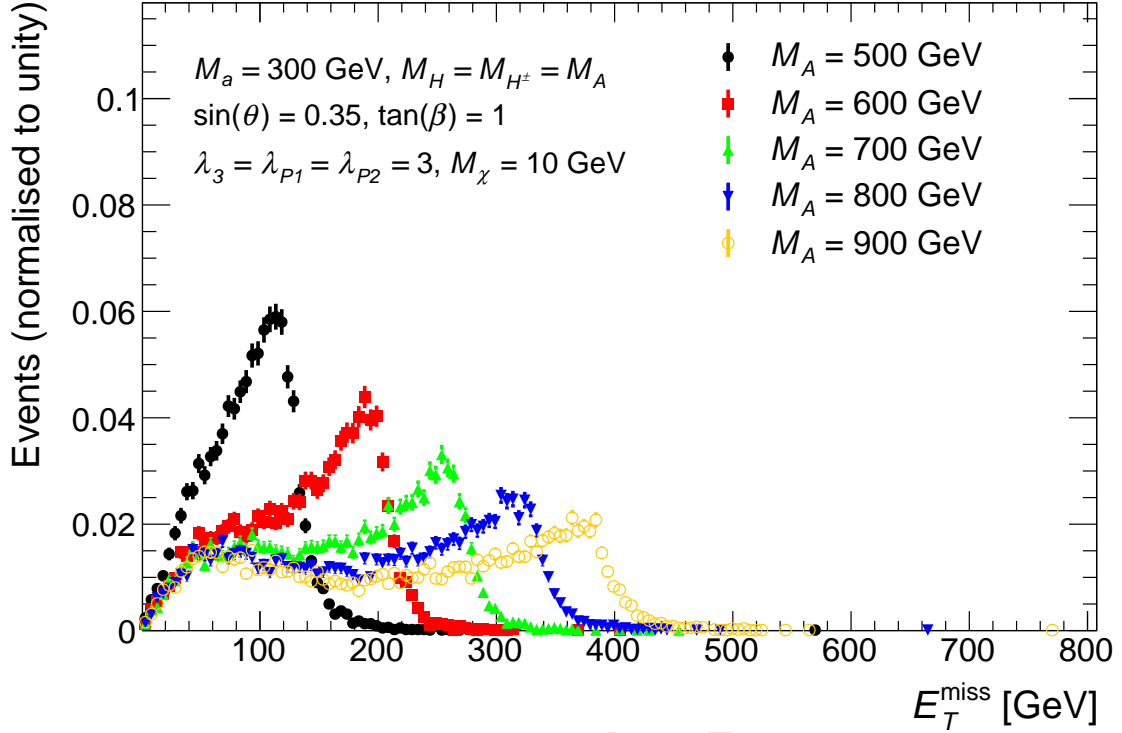


Figure 2: Missing transverse momentum distribution $h \rightarrow bb + E_T^{\text{miss}}$ signal events at parton level for five representative models with different $M_A (= M_H = M_{H^\pm})$ and fixed $M_a = 300$ GeV, $\sin \theta = 0.35$, $\tan \beta = 1$, $M_\chi = 10$ GeV and $\lambda_{P1} = \lambda_{P2} = \lambda_3 = 3$. Models with a larger $M_A - M_a$ splitting have harder E_T^{miss} (s.a. Equation 4.1).

Signal kinematics The masses M_A and M_a of the pseudoscalars A and a affect the $h(bb) + E_T^{\text{miss}}$ signal in two ways:

- by changing the location of the Jacobian peak in the E_T^{miss} distribution
- by changing the overall signal cross-section

The latter effect can be seen in Figure 8. The former is crucial to searches for $h(bb) + E_T^{\text{miss}}$ such as [?], since the E_T^{miss} observable can be used to reduce many standard model backgrounds. Standard model backgrounds are often characterized by low E_T^{miss} , unlike Dark Matter signal processes with potentially very high E_T^{miss} .

The Jacobian peak is the result of a resonantly produced pseudoscalar A decaying in the $1 \rightarrow 2$ decay $A \rightarrow ah$, where the h proceeds to decay into a mostly visible final state ($h \rightarrow b\bar{b} \rightarrow \text{hadrons}$), and the a into an invisible one ($a \rightarrow \chi\bar{\chi}$). The kinematics of $1 \rightarrow 2$ processes are fixed by the masses of the involved particles. Thus the resonant $A \rightarrow ah$ process has a sharply peaked resonance² in the invariant mass distribution of the final state system. This results in a peak in the momentum distribution of the Dark Matter

²with a finite width due to the widths of a , A and h

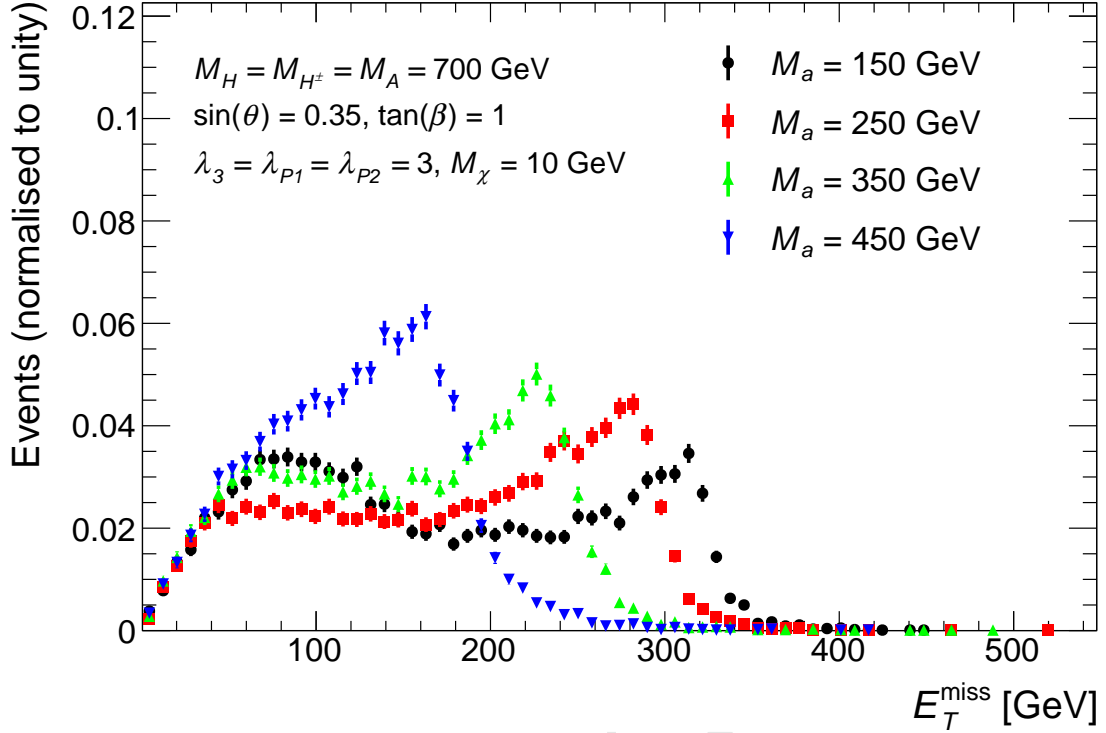


Figure 3: Missing transverse momentum distribution in $h \rightarrow bb + E_T^{\text{miss}}$ signal events at parton level for four representative models with different M_a and fixed $M_A = M_H = M_{H^\pm} = 700$ GeV, $\sin \theta = 0.35$, $\tan \beta = 1$, $M_\chi = 10$ GeV and $\lambda_{P1} = \lambda_{P2} = \lambda_3 = 3$. Models with higher M_a have softer E_T^{miss} (s.a. Equation 4.1).

system, and the transverse component of the Dark Matter momentum is reconstructed as the missing transverse momentum (E_T^{miss}). This peak in the E_T^{miss} distribution resulting from the resonant signal process is called the Jacobian peak.

Since it is determined by the masses of the particle involved in the signal process, the location of the Jacobian peak can be calculated analytically [?]:

$$E_T^{\text{miss}, \text{max}} \approx \frac{\sqrt{(M_A^2 - M_a^2 - M_h^2)^2 - 4M_a^2 M_h^2}}{2M_A} \quad (4.1)$$

Thus increasing M_A leads to a Jacobian peak at higher E_T^{miss} , and vice versa (Figure 2). Conversely, models with higher M_a have a Jacobian peak at lower E_T^{miss} , and vice versa (Figure 3). Because they determine the location of the Jacobian peak, M_A and M_a strongly affect the sensitivity of a search for $h(bb) + E_T^{\text{miss}}$ to a given model. For this reason, one of the proposed parameter scans for the 2HDM with pseudoscalar Dark Matter mediator is a scan in the (M_a, M_A) plane.

Some fraction of signal events is due to non-resonant $2 \rightarrow 3$ processes $gg \rightarrow h\chi\bar{\chi}$. Due to the larger number of kinematic degrees of freedom, these processes have a broadly distributed invariant mass of the final state system. This in turn generates a broad distri-

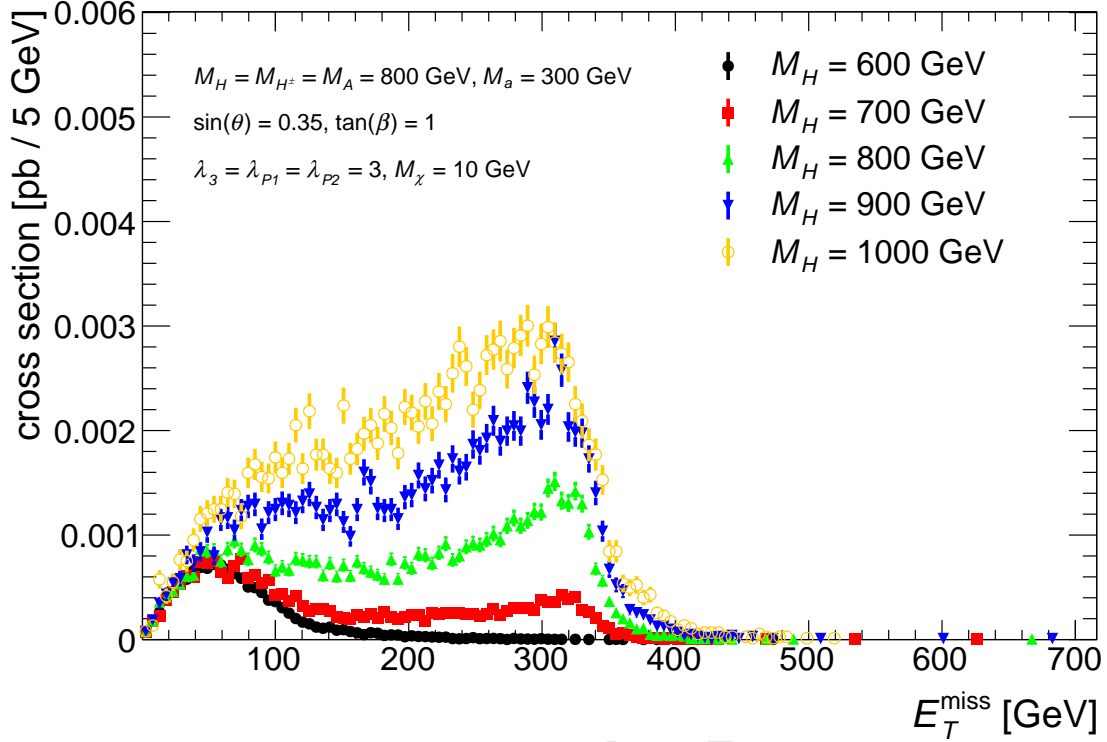


Figure 4: The E_T^{miss} distribution of the production cross section of $h \rightarrow bb + E_T^{\text{miss}}$ signal events for five representative models with different $M_H = M_{H^\pm}$ and fixed $M_A = 800$ GeV, $M_a = 300$ GeV, $\sin \theta = 0.35$, $\tan \beta = 1$, $M_\chi = 10$ GeV and $\lambda_{P1} = \lambda_{P2} = \lambda_3 = 3$.

bution dominated by soft E_T^{miss} , distinct from the Jacobian peak discussed above. All the models in Figure 2 and Figure 3 also have low- E_T^{miss} non-resonant contributions.

The mass of the heavy neutral³ scalar H has an indirect effect on the rate and kinematics of the signal. This is caused by M_H changing the widths and couplings of the pseudoscalars A and a . Changing M_H can scale the signal cross-section up or down, and change the fraction of resonant vs. non-resonant signal events (Figure 4). The choice $M_H (= M_{H^\pm}) = M_A$ gives a measurable cross-section for many signal points as well as a significant fraction of resonant signal events.

The mass M_H of the Dark Matter fermion M_χ can change the cross-section and shape of the E_T^{miss} distribution, depending on the place of M_χ in the mass hierarchy (Figure 5). If the Dark Matter is above the production threshold ($M_\chi < M_a/2$), changing it has no effect on either kinematics or cross-section. The only exception is the case $M_a/2 > M_\chi > M_a/2 - M_h$ (given a sufficiently heavy scalar a). With such values of M_χ non-resonantly producing an h simultaneously with an on-shell $a(\rightarrow \chi\bar{\chi})$ becomes kinematically forbidden. However, this contribution is negligible for most of the parameter points in the scans presented here. If the Dark Matter is on threshold ($M_\chi = M_a/2$), the signal cross section is significantly enhanced. This enhancement on threshold drops off rapidly towards both

³For simplicity, we only consider the case of the neutral scalar H^\pm being mass-degenerate to H .

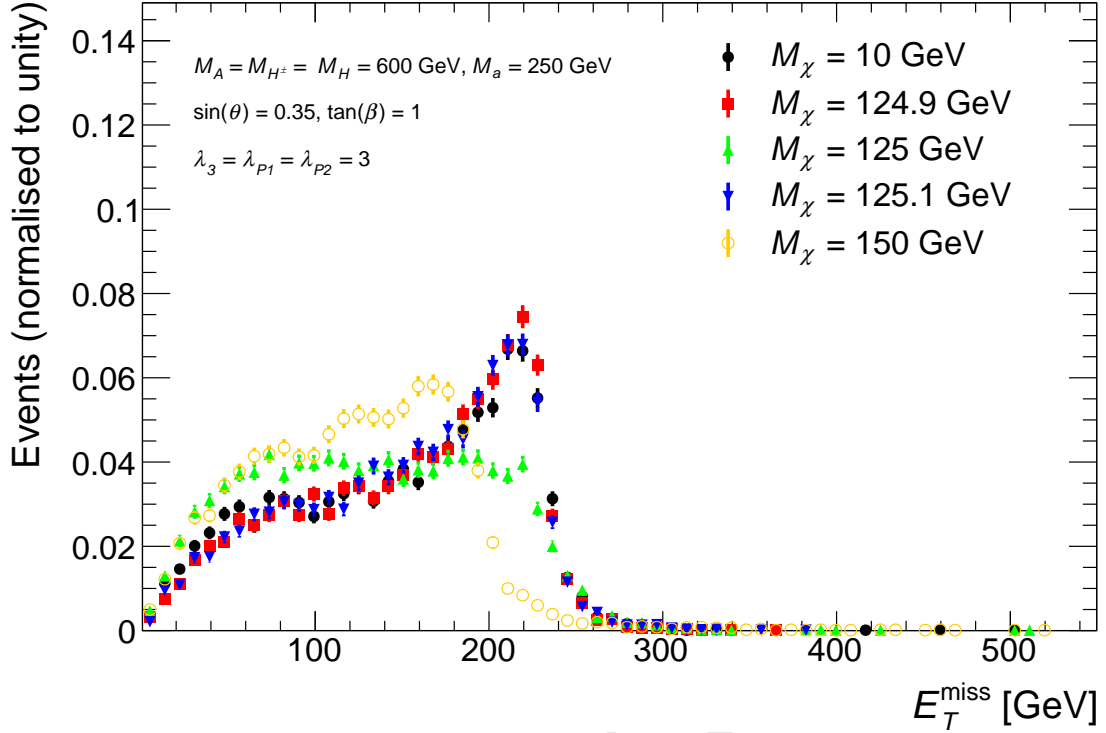


Figure 5: Missing transverse momentum distribution of $h \rightarrow bb + E_T^{\text{miss}}$ signal events at parton level for five representative models with different M_χ and fixed $M_A = M_H = M_{H^\pm} = 600$ GeV, $M_a = 250$ GeV, $\sin \theta = 0.35$, $\tan \beta = 1$ and $\lambda_{P1} = \lambda_{P2} = \lambda_3 = 3$. The shape of the E_T^{miss} distribution does not change for $M_\chi < M_a/2$, then changes significantly for $M_\chi \geq M_a/2$.

higher and lower M_χ . Furthermore, the shape of the E_T^{miss} distribution at threshold differs significantly from the one below threshold, since amplitudes involving decays $a \rightarrow \chi\bar{\chi}$ make up a larger fraction of all signal events. Below threshold ($M_\chi > M_a/2$), the signal cross-section quickly drops by several orders of magnitude. In this regime, the shape of the E_T^{miss} distribution changes with M_χ continuously.

The sine of the mixing angle between the two pseudoscalars A and a , $\sin \theta$, affects not only the cross section, but also the shape of the E_T^{miss} distribution (Figure 6). For the resonant diagram $gg \rightarrow A \rightarrow ah \rightarrow \chi\bar{\chi}h$, the product of cross section times branching ratios $\mathcal{B}(A \rightarrow ah)\mathcal{B}(a \rightarrow \chi\bar{\chi})$ scales with $\sin^2 \theta \cos^6 \theta$, while for the diagram $gg \rightarrow a \rightarrow A^*h \rightarrow \chi\bar{\chi}h$, the product of cross section times branching ratios $\mathcal{B}(a \rightarrow A^*h)\mathcal{B}(A \rightarrow \chi\bar{\chi})$ scales with $\sin^6 \theta \cos^2 \theta$. Therefore, at small $\sin \theta$, the resonant diagram $A \rightarrow ah$ is the dominant production mode and the E_T^{miss} distribution has a Jacobian peak following Equation 4.1; while at large $\sin \theta$, the $a \rightarrow A^*h$ diagram starts to dominate and produces a second peak at a lower E_T^{miss} value.

The shape of E_T^{miss} distribution also has a non-trivial dependence on $\tan \beta$ (Figure 7). As discussed in the sensitivity study later, at small $\tan \beta$, the Yukawa coupling to top

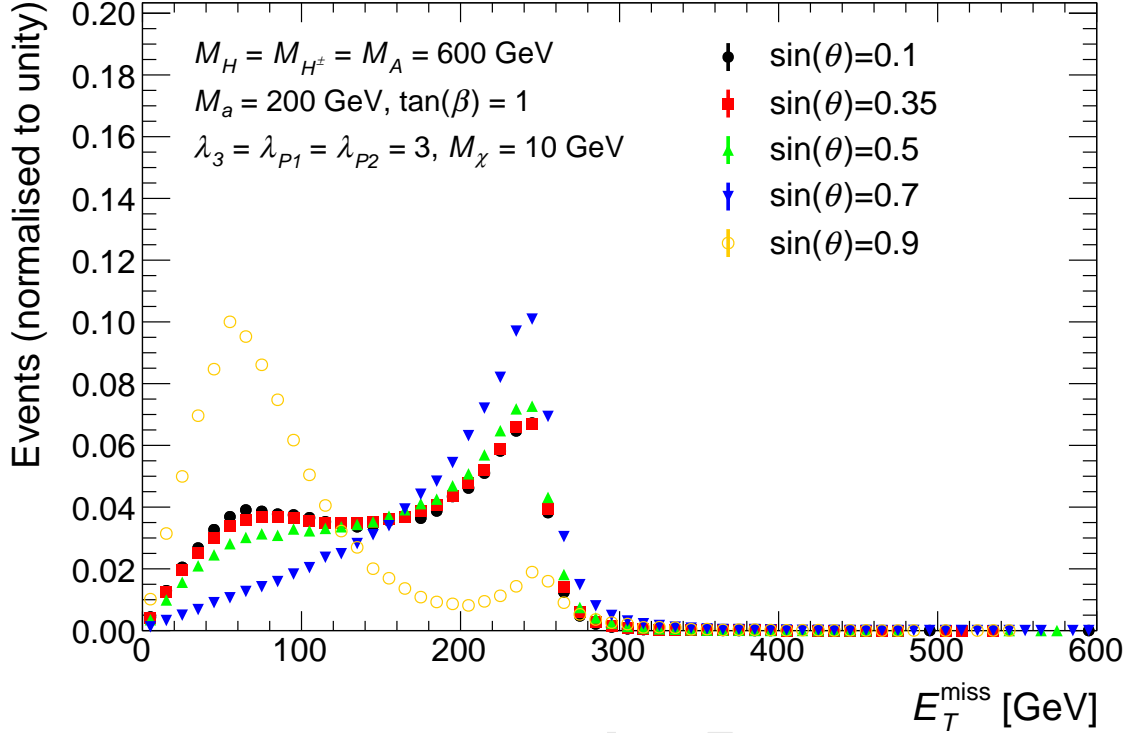


Figure 6: Missing transverse momentum distribution of $h \rightarrow bb + E_T^{\text{miss}}$ signal events at parton level for five representative models with different $\sin \theta$ and fixed $M_A = M_H = M_{H^\pm} = 600$ GeV, $M_a = 200$ GeV, $M_\chi = 10$ GeV, $\tan \beta = 1$, and $\lambda_{P1} = \lambda_{P2} = \lambda_3 = 3$. The shape of the E_T^{miss} distribution does not change much for $\sin \theta < 0.7$, then changes significantly for $\sin \theta \geq 0.7$. When $\sin \theta = 0.9$, the diagram $gg \rightarrow a \rightarrow A^* h \rightarrow \chi \bar{\chi} h$, producing a E_T^{miss} peak at around 60 GeV, starts to dominate.

quark is large and the signal production mode is dominated by the non-resonant 3-body processes $gg \rightarrow h \chi \bar{\chi}$, which gives a broad and soft E_T^{miss} spectrum. As $\tan \beta$ increases, the contribution of resonant production increases as well and the Jacobian peak also appears. When the pseudoscalar A is produced off-shell, i.e. when $M_A < M_a + M_h$, the shapes of E_T^{miss} distributions become similar and the dependence on $\tan \beta$ disappears.

Sensitivity estimate The sensitivity of the search for $h(bb) + E_T^{\text{miss}}$ described in [?] to the 2HDM with pseudoscalar Dark Matter mediator is estimated based on the limits with minimal model dependence from [?]. This allows one to directly use parton-level simulations of the 2HDM with pseudoscalar Dark Matter mediator as inputs for the estimate. Since there is no need to simulate the detector response, which is very costly in terms of CPU-time, the sensitivity can be estimated quickly. In this way, more iterations on different versions of the signal grid can be performed.

The limits with minimal model dependence are given in [?] in terms of the visible cross-section of $h(bb) + E_T^{\text{miss}}$ events. To compare these values to the parton level simulation results, an estimate of the detector efficiency as well as the acceptance of the event

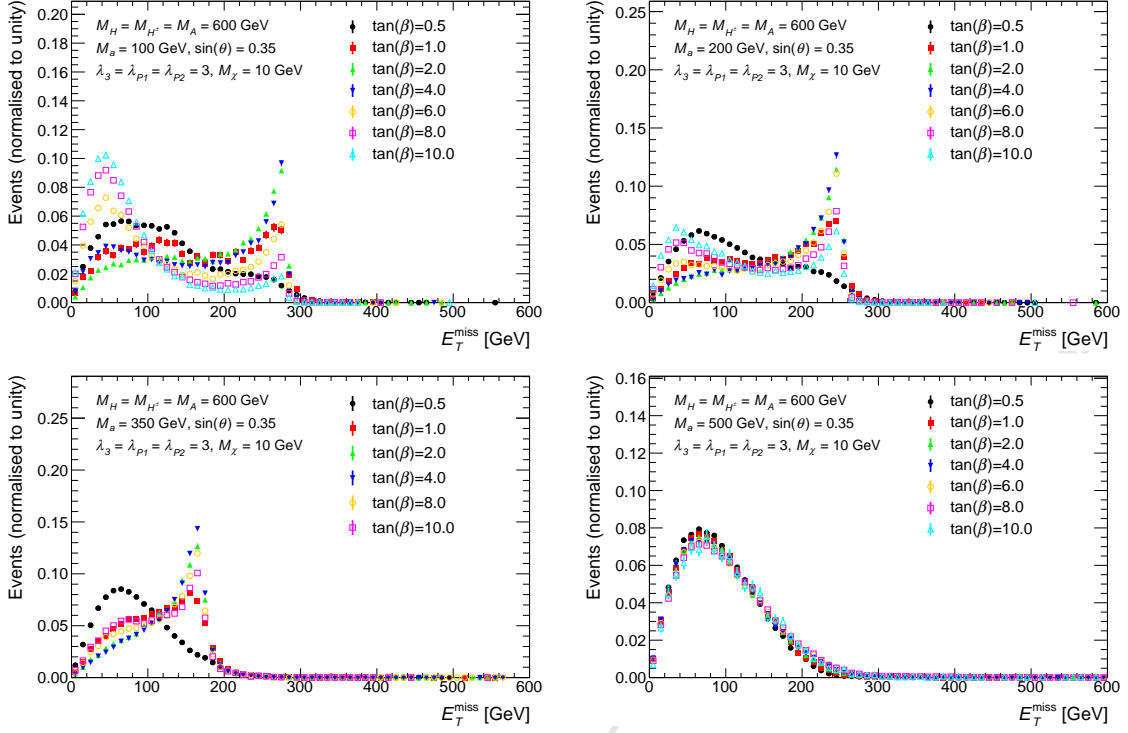


Figure 7: Missing transverse momentum distribution of $h \rightarrow bb + E_T^{\text{miss}}$ signal events at parton level with different $\tan\beta$ and fixed $M_A = M_H = M_{H^\pm} = 600$ GeV, $M_\chi = 10$ GeV, $\sin\theta = 0.35$, and $\lambda_{P1} = \lambda_{P2} = \lambda_3 = 3$. The values of M_a are set to 100, 200, 350, and 500 GeV, respectively. The shapes of the E_T^{miss} distributions for different $\tan\beta$ are similar when $M_A < M_h + M_a$. Note, in these figures, both the contributions of gg and $b\bar{b}$ initiated processes are included and a combined histogram is produced according to their corresponding cross sections.

selections of the analysis is needed. This estimate is provided in [?] in terms of a single acceptance times efficiency ($\mathcal{A} \times \epsilon$) value per E_T^{miss} bin. The value of $\mathcal{A} \times \epsilon$ corresponds to the probability that an event generated at parton level in a given E_T^{miss} bin is reconstructed in that same E_T^{miss} bin and passes all selections. The limits with minimal model dependence are provided separately for each of the four E_T^{miss} bins used in [?]. Thus, the simulated events are binned into those bins (Figure 8). Then the simulated cross-section in one E_T^{miss} bin is compared to the limit with minimal model dependence in that E_T^{miss} bin (Figure 9). In this way, one gets four separate sensitivity estimates. To obtain a single number estimating the sensitivity of a search that uses all four E_T^{miss} bins, the individual

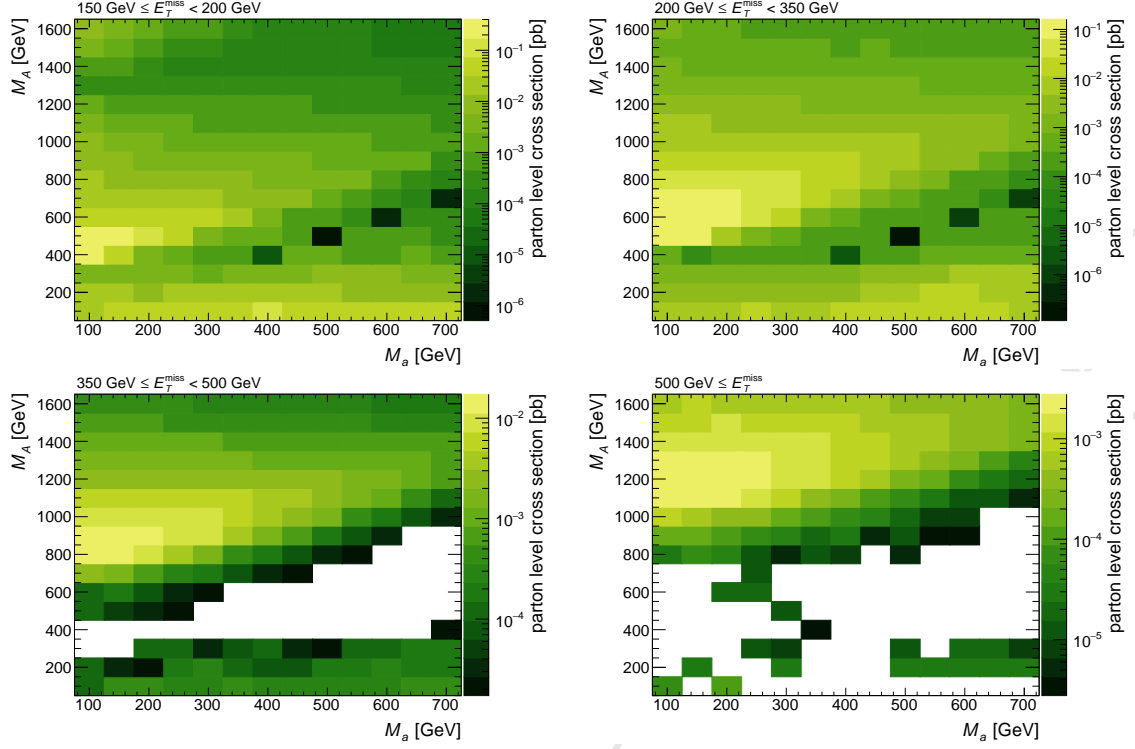


Figure 8: The production cross-section of $h \rightarrow bb + E_T^{\text{miss}}$ signal events at parton level as a function of (M_A, M_a) in each of the four E_T^{miss} bins. The remaining parameters take the values $M_H = M_{H^\pm} = M_A$, $\sin \theta = 0.35$, $\tan \beta = 1$, $M_\chi = 10$ GeV and $\lambda_{P1} = \lambda_{P2} = \lambda_3 = 3$.

contributions are summed⁴ (Figure 10). Thus the sensitivity is estimated as

$$\begin{aligned}
 S^m &= \sum_i^{E_T^{\text{miss}} - \text{bins}} S_i^m \\
 &= \sum_i^{E_T^{\text{miss}} - \text{bins}} \frac{\sigma_i^{m, \text{parton}}(h\chi\bar{\chi}) \times \mathcal{BR}_{\text{SM}}(h \rightarrow b\bar{b}) \times [\mathcal{A} \times \epsilon]_i}{\sigma_i^{\text{observed}}(h(bb) + E_T^{\text{miss}})},
 \end{aligned} \tag{4.2}$$

where m is a particular model, i is a particular E_T^{miss} bin, S_i^m the sensitivity to model m based on E_T^{miss} -bin i (Figure 9), $\sigma_i^{m, \text{parton}}(h\chi\bar{\chi})$ the parton level $h\chi\bar{\chi}$ production cross-section in bin i predicted by model m (Figure 8), $\mathcal{BR}_{\text{SM}}(h \rightarrow b\bar{b})$ the $h \rightarrow b\bar{b}$ branching ratio predicted by the standard model for $M_h = 125$ GeV, $[\mathcal{A} \times \epsilon]_i$ the acceptance times efficiency in bin i as given in [?], and $\sigma_i^{\text{observed}}(h(bb) + E_T^{\text{miss}})$ the limit on the $h(bb) + E_T^{\text{miss}}$ cross-section observed in [?] in E_T^{miss} bin i .

⁴This implies that there could be models where the sensitivity in every bin is < 1 , yet the sum is > 1 . This is desired for the purpose of estimating sensitivity when designing the grid to be used in a dedicated search, since one expects that the full search will be able to exclude those models. But for actually excluding models based on the limits with minimal model dependence, the sum is not appropriate. A better choice for the purpose of exclusion is e.g. the sensitivity of the most sensitive bin.

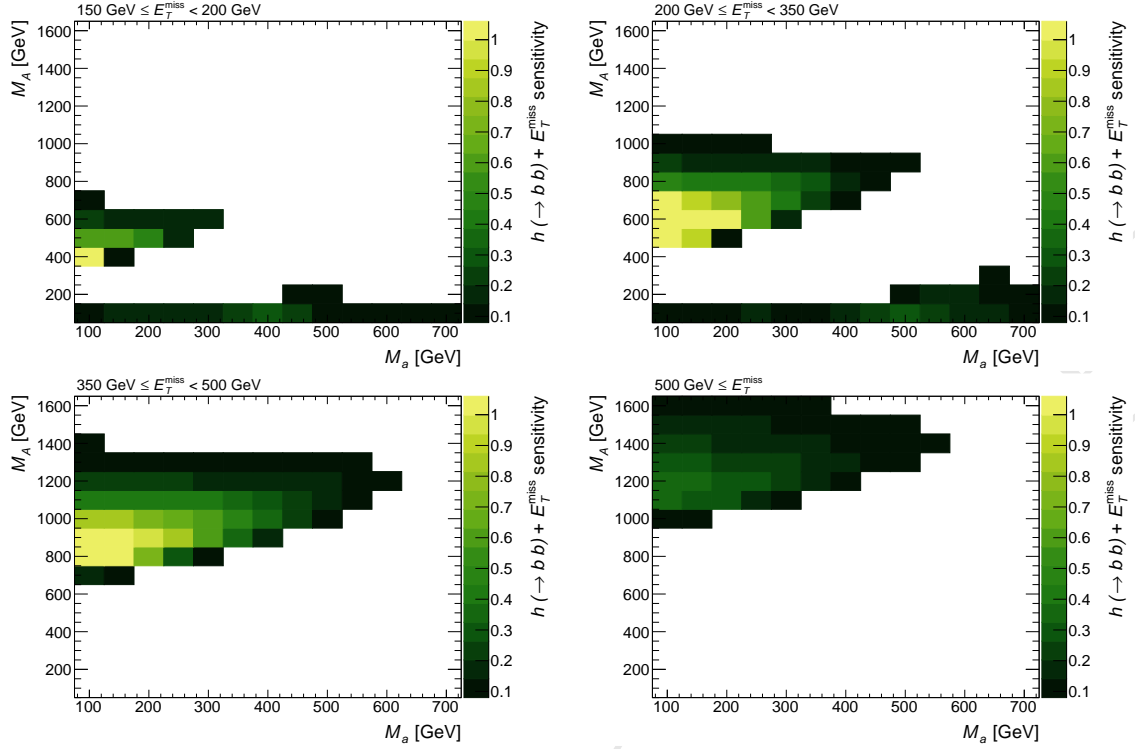


Figure 9: Estimated sensitivity to $h \rightarrow bb + E_T^{\text{miss}}$ events as a function of (M_A, M_a) in each of the four E_T^{miss} bins. The sensitivity, defined in Eq. 4.2, is based on the limits with reduced model dependence from Ref. [?]. The remaining parameters take the values $M_H = M_{H^\pm} = M_A$, $\sin \theta = 0.35$, $\tan \beta = 1$, $M_\chi = 10$ GeV and $\lambda_{P1} = \lambda_{P2} = \lambda_3 = 3$.

The $h(bb) + E_T^{\text{miss}}$ sensitivity in the sense of eq. 4.2 to a scan in the (M_a, M_A) plane is shown in Figure 9. The sensitivity drops with increasing $M_A = M_H = M_{H^\pm}$ for $M_A \geq 1$ TeV because the fraction of resonant signal events drops. The drop in the fraction of resonant signal events is caused by increasingly large Γ_A , which allows an increasing fraction of non-resonant signal events, driven by events with very off-shell A . Non-resonant signal events have soft E_T^{miss} and thus the search is less sensitive to them, since the minimum accepted E_T^{miss} is $E_T^{\text{miss}} \geq 150$ GeV. Near the mass diagonal $M_a = M_A$, there is little to no sensitivity. This is because the Jacobian peak is at soft E_T^{miss} for a low mass-splitting $M_A - M_a$ (Equation 4.1, Figure 2, and Figure 3). Furthermore the coupling $g_A ah$ is small when all Higgs bosons are nearly mass degenerate [?], giving a small total cross-section, and lowering the sensitivity even further. The sensitivity above the mass diagonal ($M_A > M_a$) is larger than the sensitivity below the mass diagonal ($M_A < M_a$). Two parameter choices cause this asymmetry:

1. $M_A = M_H = M_{H^\pm}$, i.e. the neutral and charged CP-even scalars have low masses below the diagonal, but high masses above it, introducing asymmetry. In Figure 4 one can see that values of $M_H = M_{H^\pm}$ below the mass of the higher-mass pseudoscalar give a reduced overall cross-section and a lower fraction of resonant signal events. Both effects reduce sensitivity.

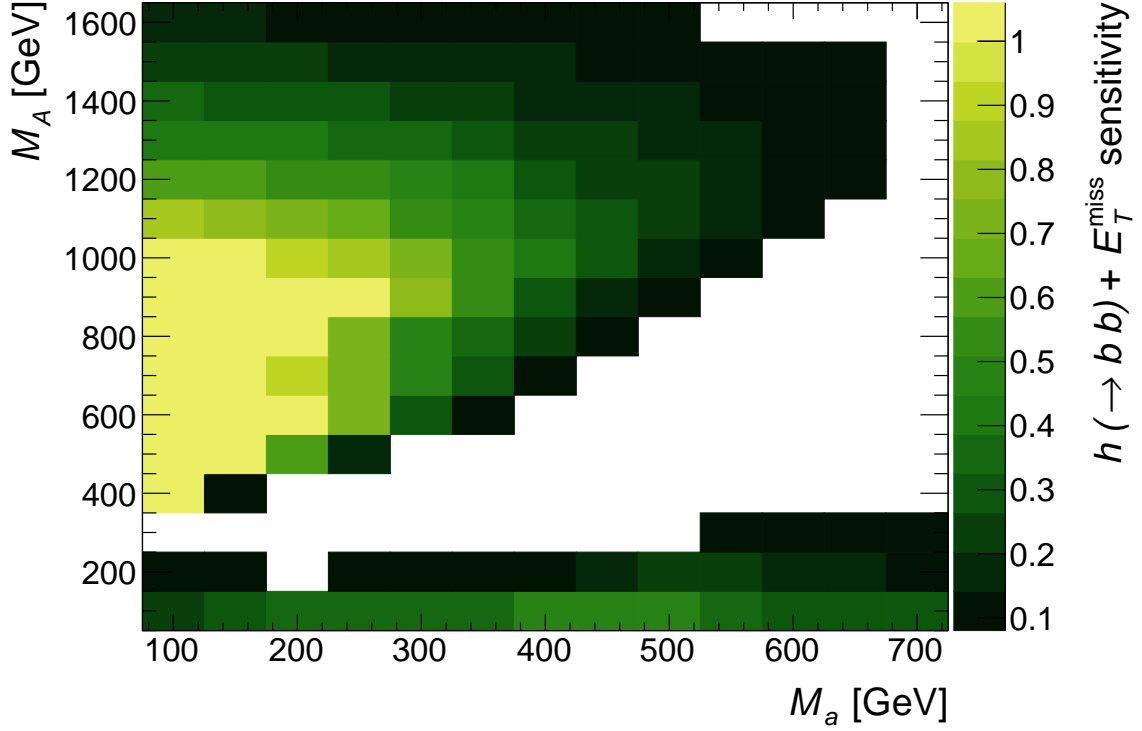


Figure 10: Sum over all E_T^{miss} -bins of the estimated sensitivity to $h \rightarrow bb + E_T^{\text{miss}}$ events as a function of (M_A, M_a) . The sensitivity, defined in Eq. 4.2, is based on the limits with reduced model dependence from Ref. [?]. The remaining parameters take the values $M_H = M_{H^\pm} = M_A$, $\sin \theta = 0.35$, $\tan \beta = 1$, $M_\chi = 10$ GeV and $\lambda_{P1} = \lambda_{P2} = \lambda_3 = 3$.

2. $\sin \theta = 0.35 \neq 1/\sqrt{2}$, i.e. the pseudoscalar mixing is asymmetric. A couples comparatively more strongly to SM particles than a , and vice versa for the couplings to the Dark Matter fermion χ . So the situation below the diagonal corresponds to the case of $\sin \theta = \sqrt{1 - 0.35^2} \approx 0.938$ and $M_A > M_a$. As can be seen in ?? and ?? this configuration has a larger fraction of soft, nonresonant signal events, and correspondingly lower sensitivity (Figure 13 and Figure 14).

For a scan in $(M_a, \tan \beta)$ the sensitivity is shown in Figure 11. At very low $\tan \beta$, the yukawa coupling to top quarks is large, and most of the signal events come from non-resonant processes. The non-resonant processes give soft E_T^{miss} , which lowers the signal acceptance and reduces the sensitivity of the search. For higher $\tan \beta$ the fraction of resonant events increases, due to the reduced top Yukawa coupling, increasing the sensitivity. However reducing the top yukawa coupling also reduces the overall production cross-section. This effect is sub-dominant below $\tan \beta \approx 1.2$, and the sensitivity increases with $\tan \beta$. But above $\tan \beta \approx 1.2$, the sensitivity loss due to reduced cross-section outpaces the sensitivity gain due to a more resonant signal. Therefore, above $\tan \beta \approx 1.2$, the search gets less sensitive with higher $\tan \beta$. At very high $\tan \beta (\geq 10)$, this trend is reversed again, as the $\tan \beta$

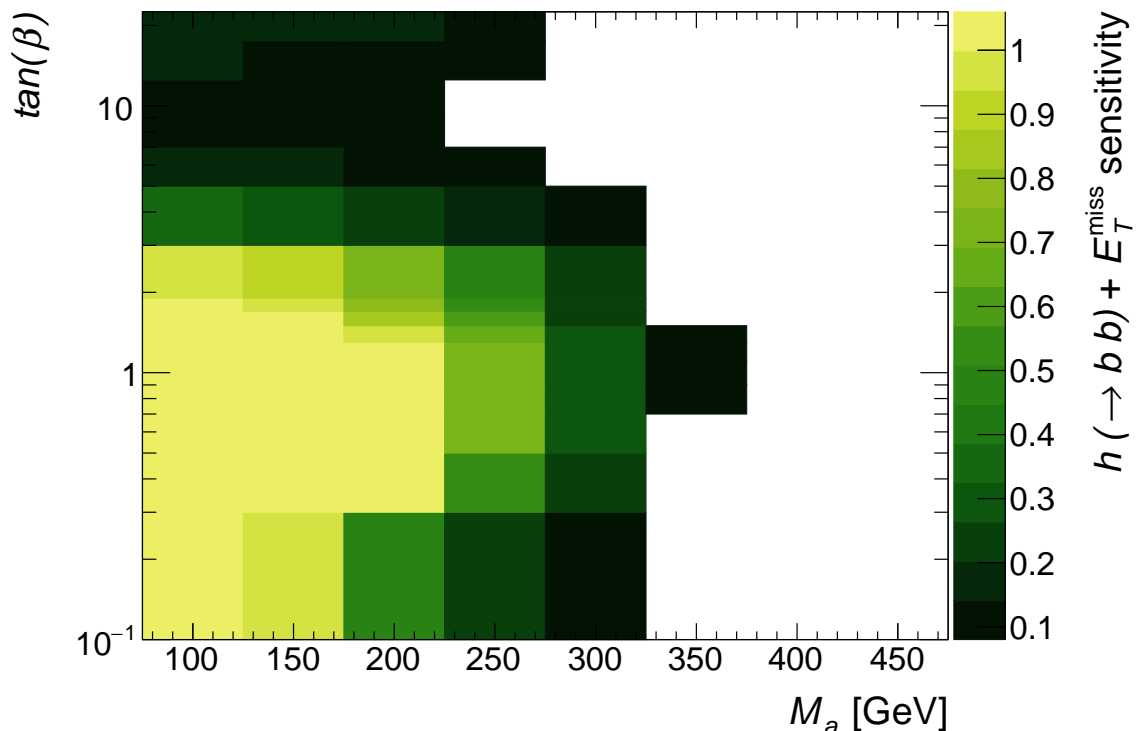


Figure 11: Sum over all E_T^{miss} -bins of the estimated signal sensitivity to $h \rightarrow bb + E_T^{\text{miss}}$ events as a function of $(M_a, \tan \beta)$. The sensitivity, defined in Eq. 4.2, is based on the limits with reduced model dependence from Ref. [?]. The remaining parameters take the values $M_H = M_{H^\pm} = M_A = 600$ GeV, $\sin \theta = 0.35$, $M_\chi = 10$ GeV and $\lambda_{P1} = \lambda_{P2} = \lambda_3 = 3$.

enhancement⁵ of the coupling to b-quarks relative to top quarks becomes so large that it compensates for the lower b quark Yukawa coupling corresponding to the lower b-quark mass. At this point $b\bar{b}$ initiated processes start to dominate the production cross-section and drive the increase in sensitivity.

The sensitivity to models with varying $\sin \theta$ is shown in Figs. 13 and 14. The sensitivity is 0 at $\sin \theta = 0$ and $\sin \theta = 1$, since those values correspond to no mixing, and thus no coupling. So the sensitivity is in general not monotonous in $\sin \theta$ (Figure 13). For intermediate values, $\sin \theta$ influences the couplings of the pseudoscalars to Dark Matter, as well as to standard model fermions, and also the coupling strength of trilinear scalar vertices such as g_{Aah} [?]. Increasing the couplings increases the cross-section and thereby the sensitivity. However, increasing some couplings can also increase Γ_A and thereby decrease the resonant fraction of signal events. This means that there can be more than one local maximum in the sensitivity curve (Figure 14). The number and location of maxima and turning points in the sensitivity depends on the precise interplay of the couplings. The couplings depend on all other model parameters including all the Higgs masses, so tuning the $\sin \theta$ of a parameter scan to the sensitivity in a single point can lead to sub-optimal

⁵we are considering a Yukawa sector of type II

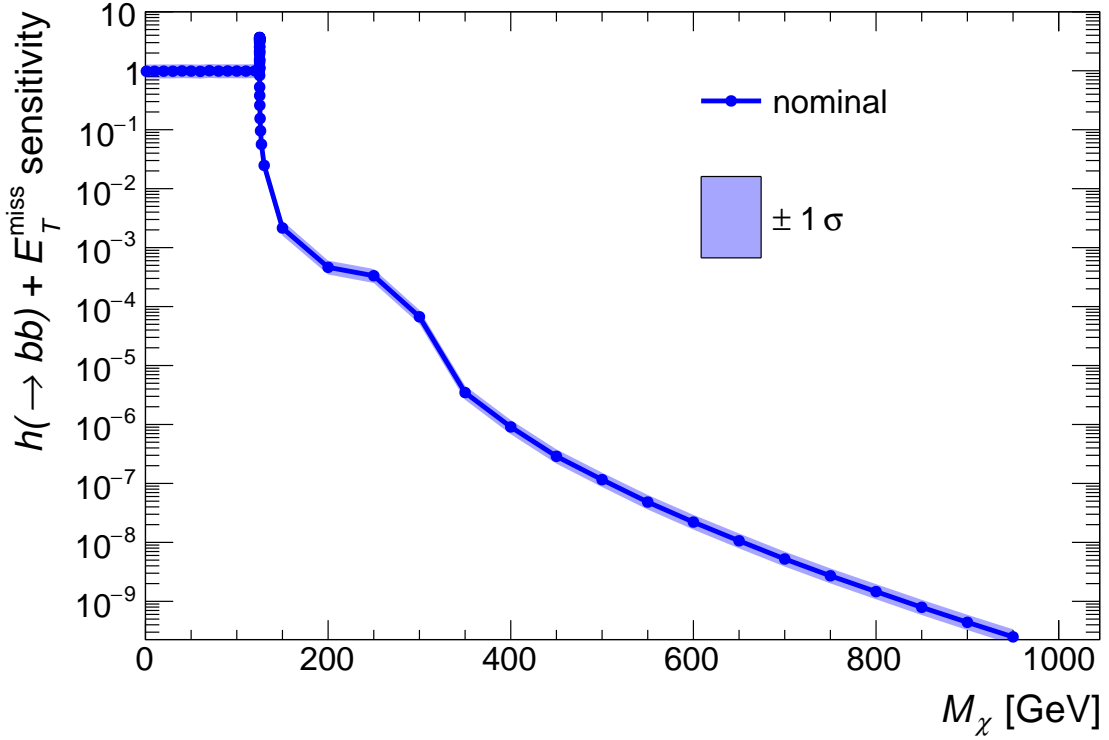


Figure 12: Sum over all E_T^{miss} -bins of the estimated signal sensitivity to $h \rightarrow bb + E_T^{\text{miss}}$ events as a function of the Dark Matter mass M_χ . The sensitivity, defined in Eq. 4.2, as well as the uncertainty on the sensitivity (shaded blue) are based on the limits with reduced model dependence from Ref. [?] and the uncertainties described therein. The remaining parameters take the values $M_a = 250$ GeV, $M_H = M_{H^\pm} = M_A = 600$ GeV, $\sin \theta = 0.35$, $\tan \beta = 1$, and $\lambda_{P1} = \lambda_{P2} = \lambda_3 = 3$. The sensitivity is constant below $M_\chi < M_a/2$, and rapidly drops for $M_\chi > M_a/2$. The sensitivity is enhanced for $M_\chi = M_a/2$.

sensitivity in other points.

The sensitivity to models with varying M_χ is shown in Figure 12. Above threshold ($M_\chi < M_a/2$), the sensitivity stays constant. This constant sensitivity results from the constant signal E_T^{miss} shape (Figure 5), and the constant signal cross-section. At threshold ($M_\chi = M_a$) the sensitivity is enhanced because the partial width for $a \rightarrow \chi\bar{\chi}$ is enhanced, increasing the signal cross-section. Below threshold ($M_\chi > M_a/2$), the sensitivity drops rapidly. The reason for the rapid drop in sensitivity is that $M_\chi > M_a/2$ requires a virtual $a^* \rightarrow \chi\bar{\chi}$ decay in the signal event. The rate of this virtual a decay is strongly suppressed by the typically narrow width of a . The width of a is substantially reduced once $a \rightarrow \chi\bar{\chi}$ is kinematically inaccessible, as $\Gamma_{a \rightarrow \chi\bar{\chi}}$ is a large contribution to the total width of a for $M_\chi \leq M_a/2$ [?]. There is a slight bump in sensitivity for $M_\chi \approx M_A/2$, when the $A \rightarrow \chi\bar{\chi}$ hits its threshold, but the absolute sensitivity remains negligible.

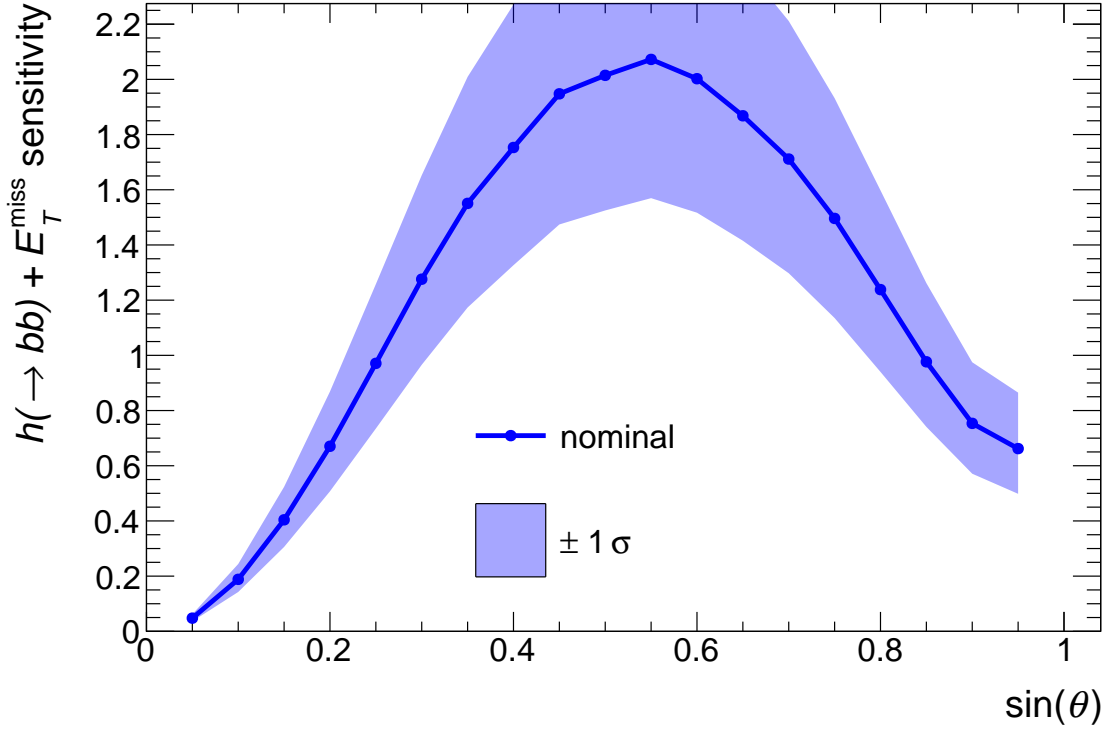


Figure 13: Sum over all E_T^{miss} -bins of the estimated signal sensitivity to $h \rightarrow bb + E_T^{\text{miss}}$ events as a function of the pseudoscalar mixing parameter $\sin \theta$. The sensitivity, defined in Eq. 4.2, as well as the uncertainty on the sensitivity (shaded blue) are based on the limits with reduced model dependence from Ref. [?] and the uncertainties described therein. The remaining parameters take the values $M_a = 200$ GeV, $M_H = M_{H^\pm} = M_A = 600$ GeV, $M_\chi = 10$ GeV, $\tan \beta = 1$, and $\lambda_{P1} = \lambda_{P2} = \lambda_3 = 3$.

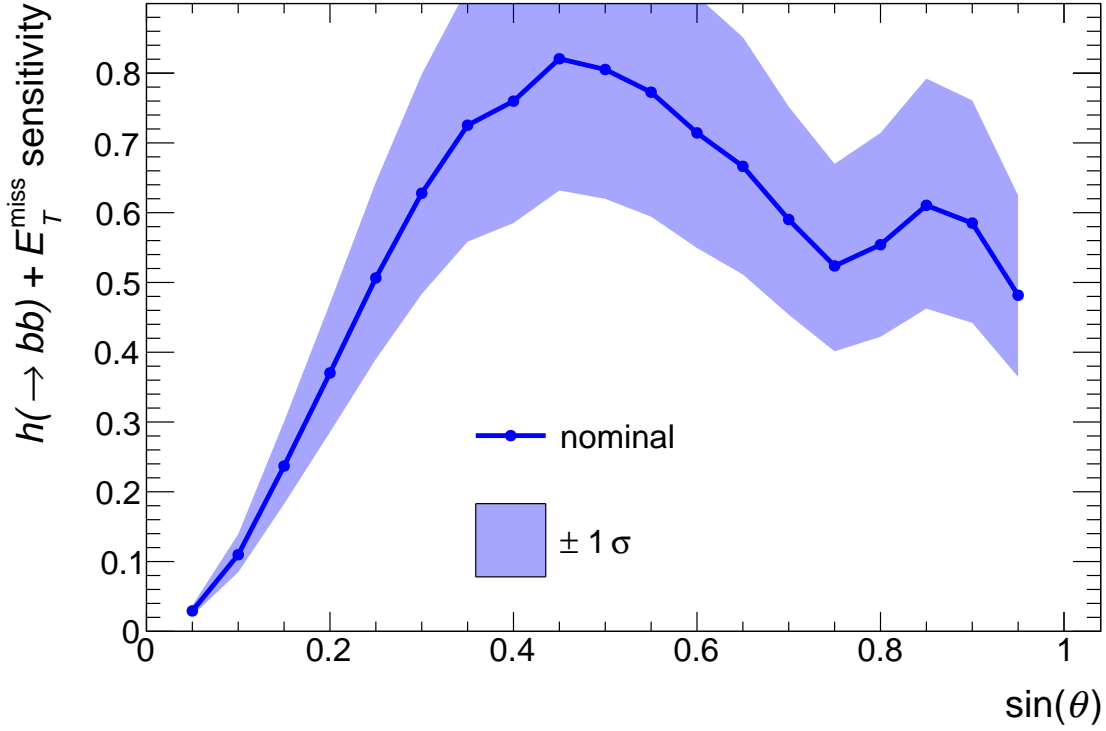


Figure 14: Sum over all E_T^{miss} -bins of the estimated signal sensitivity to $h \rightarrow bb + E_T^{\text{miss}}$ events as a function of the pseudoscalar mixing parameter $\sin \theta$. The sensitivity, defined in Eq. 4.2, as well as the uncertainty on the sensitivity (shaded blue) are based on the limits with reduced model dependence from Ref. [?] and the uncertainties described therein. The remaining parameters take the values $M_a = 350$ GeV, $M_H = M_{H^\pm} = M_A = 1000$ GeV, $M_\chi = 10$ GeV, $\tan \beta = 1$, and $\lambda_{P1} = \lambda_{P2} = \lambda_3 = 3$.

4.1.3 Studies of the mono-Z (leptonic) signature

Technical setup Simulated event samples for the mono-Z signature are produced with Madgraph5_aMC@NLO version 2.4.3, interfaced with Pythia version 8.2.2.6 for parton showering. The NNPDF3.0 PDF set is used at LO precision with the value of the strong coupling constant set to $\alpha_S(M_Z) = 0.130$ (NNPDF30_lo_as.0130). Only contributions from gluon-gluon initial states and $l^+ l^- \chi\bar{\chi}$ final states are considered, where $l = e$ or μ . No additional matrix element partons are considered and diagrams with an intermediate s-channel SM Higgs boson are explicitly rejected to increase the calculation efficiency (generate g g > xd xd l+ l- / h1).

Event selection Three consecutive stages of event selection are considered:

- Inclusive: Lepton p_T and η requirements corresponding to the typical experimental trigger acceptance are applied.
- Preselection: A dilepton candidate with an invariant mass in a window around the Z mass is required, and a minimum transverse momentum of the $\chi\bar{\chi}$ system is required.
- Final selection: Requirements on the main variables used in the relevant analyses are added: The angular separation in the transverse plane between the $\chi\bar{\chi}$ and $l^+ l^-$ systems $\Delta\Phi(l, E_T^{\text{miss}})$, the relative transverse momentum difference between them $|p_{T,l} - E_T^{\text{miss}}|/p_{T,l}$ and the angular separation between the leptons $\Delta R(l)$. Additionally, the E_T^{miss} requirement is tightened.

The exact event selection criteria are listed in Tab. 1.

Results The overall cross-sections in the $\tan\beta$ and mass scans are shown in Fig. ???. In the mass scan, maximal cross-sections are observed for the region of $M_a < M_A$ for values of $M_a \gtrsim 100$ GeV. Towards higher values of both M_a and M_A , the cross-sections fall off, reaching values smaller than 1 fb at $M_a \approx 450$ GeV or $M_A \approx 1.1$ TeV. In the $M_a \approx M_A$ -region, the cross-section is suppressed by destructive interference. For the region with inverted mass hierarchy $M_a > M_A$, cross-sections of the order of multiple fb are observed,

Table 1: Event selection requirements for the analysis of the Mono-Z signature with leptonic Z decays. The requirements are inspired to follow those used in typical experimental analyses.

Selection stage	Quantity	Requirement
Inclusive	lepton $ \eta $	< 2.5
	leading (trailing) lepton p_T	$> 25(20)$ GeV
Preselection	$ m_{ll} - m_{Z,\text{nominal}} $	< 15 GeV
	E_T^{miss}	> 40 GeV
Final selection	$\Delta\Phi(l, E_T^{\text{miss}})$	> 2.7
	$ p_{T,l} - E_T^{\text{miss}} /p_{T,l}$	< 0.4
	$\Delta R(l)$	< 1.8

as long as $|M_a - M_A|$ remains sufficiently large. In the $\tan \beta$ scan, cross-sections smoothly fall with increasing M_a as well as $\tan \beta$. Cross-sections are typically larger than 1 fb up to $\tan \beta \approx 5$. The dependence on M_a is modulated by the value of $\tan \beta$: Crossing the M_a range from 100 to 400 GeV, cross-sections are reduced by a factor ≈ 7 for small $\tan \beta \approx 1$, but only a factor ≈ 2 for higher values of $\tan \beta \approx 5$.

To assess the kinematic behavior of the signal, the distributions of the kinematic variables that are most relevant to the Mono-Z signature are studied as a function of the model parameters.

The distribution of the invariant masses of the dilepton and $\chi\chi$ systems are shown in Fig. ???. Independent of the parameters, the dilepton mass spectrum is centered at the Z peak, without any nonresonant contribution. The $M_{\chi\chi}$ distribution illustrates the signal contributions from different diagrams. For $M_A > M_a$, DM is dominantly produced from on-shell a boson production. In the inverted mass region $M_A < M_a$, the situation is reversed, and A diagrams dominate.

After applying the preselection requirements, the distributions of kinematic variables are shown in Fig. ???. In the region of $M_A > M_a$, distinct Jacobian peaks are visible in the distributions of the mediator p_T , the width of which generally increases with the M_a and M_A . Significant portions of the spectrum are situated at relatively high boosts ($E_T^{\text{miss}} > 200 \text{ GeV}$), which is more easily accessible experimentally. This behavior is contrasted by the distributions in the inverted mass regions, which show nearly no distinct features and are mainly located at low mediator p_T . For $M_A \approx M_a + m_Z$, both the a and Z bosons are produced close to at rest, leading to an event population with overall low boost. These qualitative trends are consistent between the observables studied here. Finally, the distributions of the E_T^{miss} and M_T variables after final selection are shown in Fig. ???. Traditionally, the Mono-Z search has relied on the E_T^{miss} distribution for signal extraction. While the presence of the Jacobian peak structure in the distribution facilitates signal-background separation, it may be beneficial to also consider the M_T distribution. Although only transverse information is available, the resonant structure of the signal is significantly enhanced in the M_T variable, which may enhance the sensitivity of a specialized search strategy.

The $\tan \beta$ and $\sin(\theta)$ variables have no effect on the distributions of kinematic variables (Fig. ??).

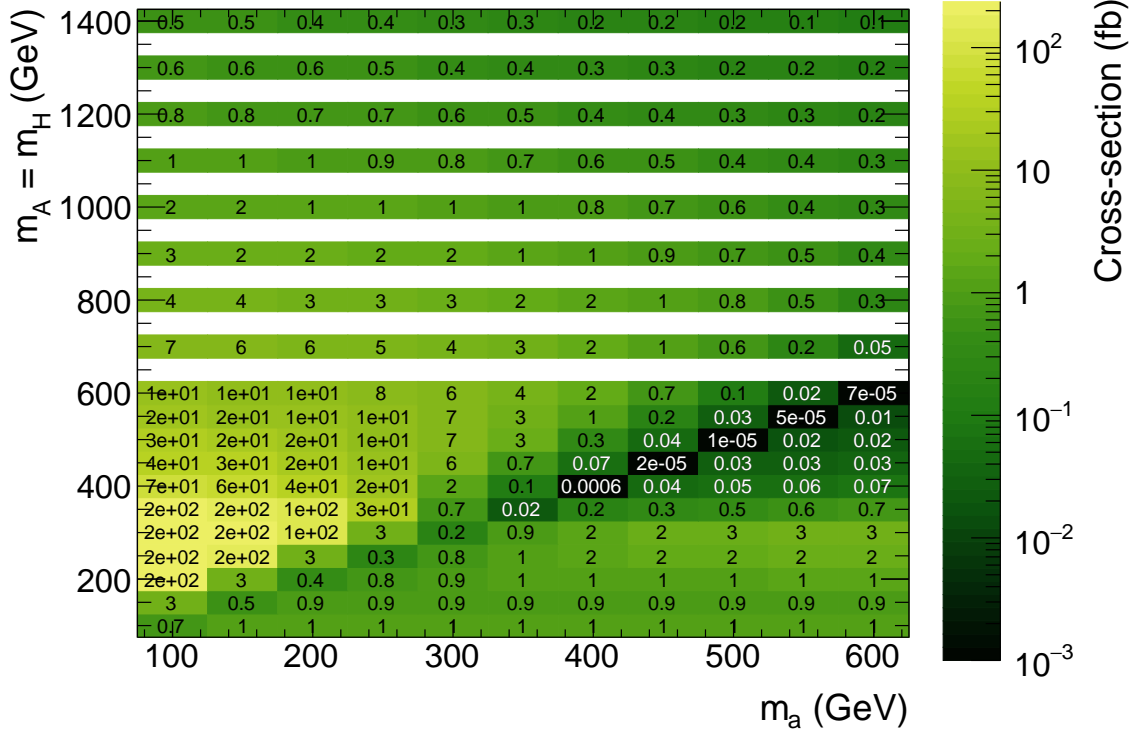


Figure 15: Inclusive cross-sections for $pp \rightarrow l^+l^-\chi\bar{\chi}$ in the M_a - M_A scan. Maximal cross-sections are observed for the region of $M_a < M_A$ for values of $M_a \gtrsim 100$ GeV. In the $M_a \approx M_A$ -region, the cross-section is suppressed by destructive interference. Finally, for a region with inverted mass hierarchy $M_a > M_A$, cross-sections of the order of multiple fb^{-1} are observed, as long as $|M_a - M_A|$ remains sufficiently large.

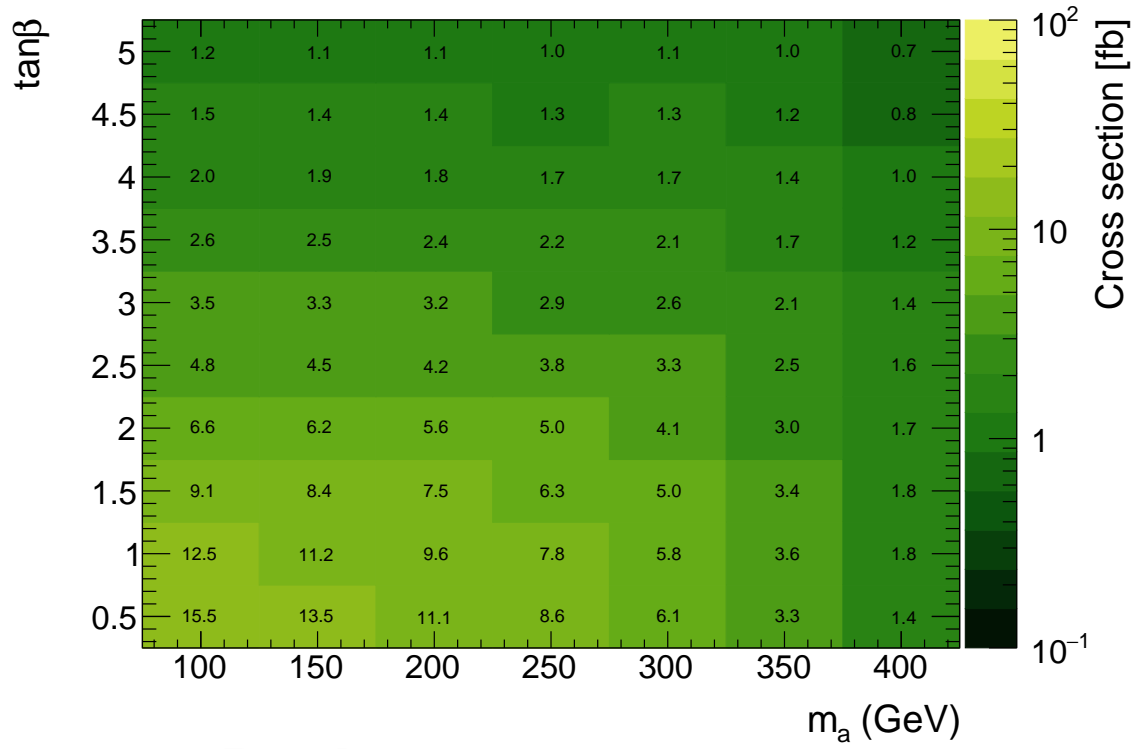


Figure 16: Inclusive cross sections for the M_a -tanBeta scan. M_A fixed to 600 GeV and sinTheta to 0.35

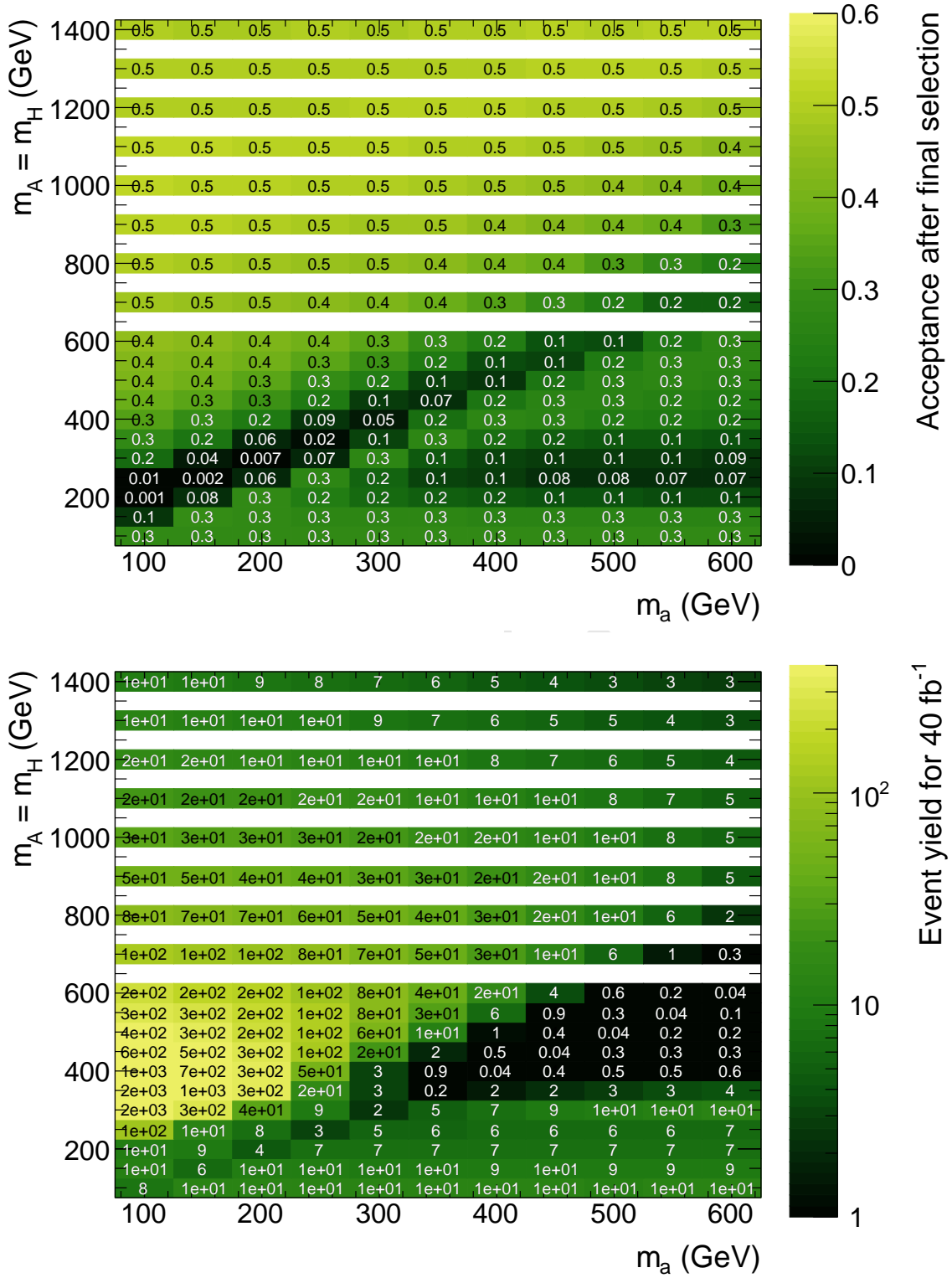


Figure 17: Acceptance and event yields in the M_a - M_A plane after applying the final selection. Event yields assume an integrated luminosity of 40 fb⁻¹. The acceptance is maximal for $M_A > M_a$, where it reaches 50 %. In the inverted mass region $M_A < M_a$, lower values of 10-30% are observed. In the intermediate region around $M_A \approx M_a + M_Z$, the acceptance is strongly suppressed as the a and Z bosons are produced approximately at rest.

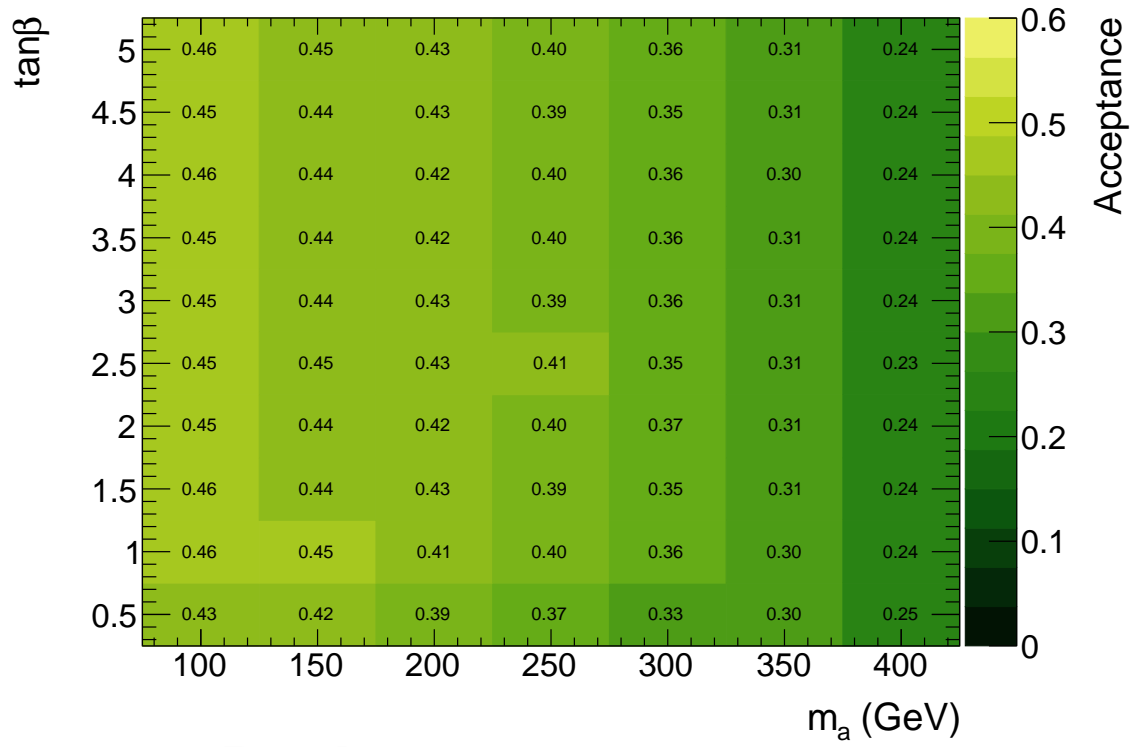


Figure 18: Acceptances across the M_a -tanBeta scan. Acceptance is flat over tanBeta for constant values of M_a .

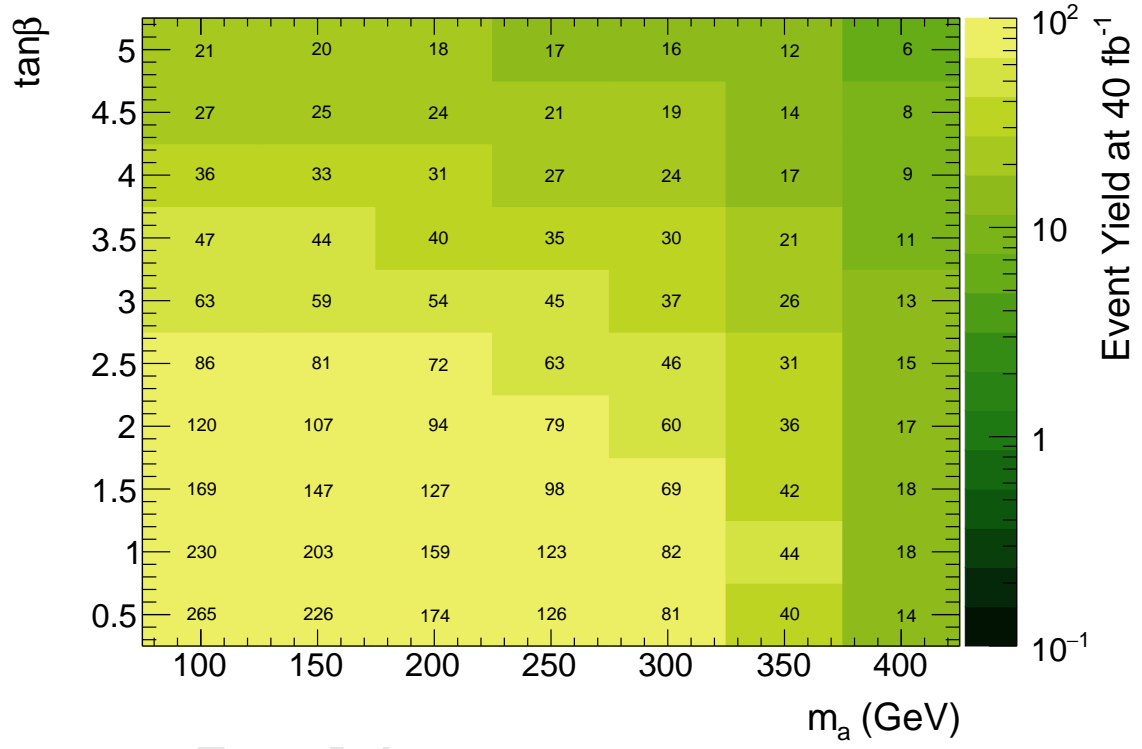


Figure 19: Event yield in the M_a -tanBeta grid, for an integrated luminosity of 40 fb^{-1} . The number of expected events diminishes with increasing tanBeta and M_a . M_A fixed to 600 GeV and sinTheta to 0.35

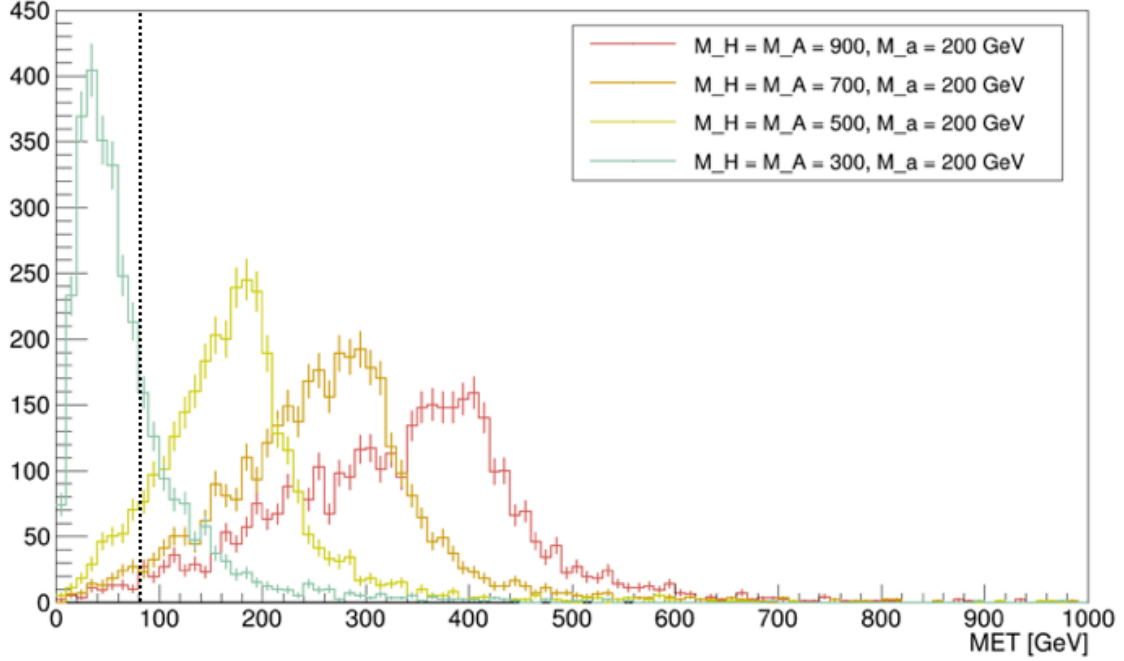


Figure 20: The position of the Jacobian peak in the E_T^{miss} distribution depends on the difference between M_H and M_a . For fixed values of M_a and $M_A = M_H$, increasing M_A shifts the peak towards higher energies, and decreasing M_A shifts it lower. For small mass splittings between M_H and M_a , most events will fail to pass the E_T^{miss} selection criteria.

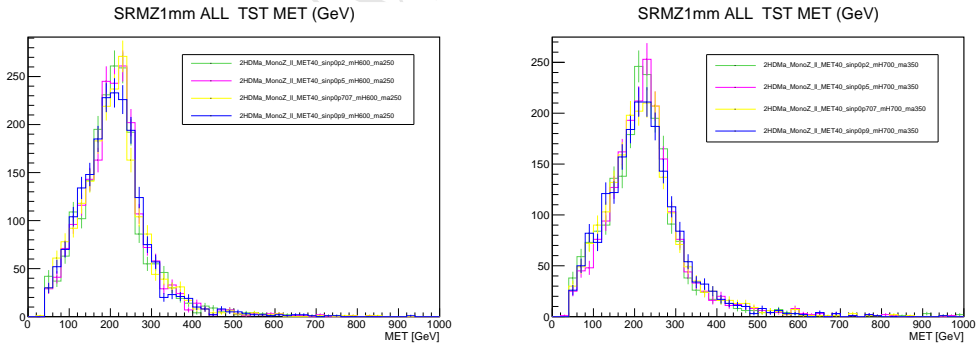


Figure 21: Performing one dimensional scans of $\sin\Theta$ shows that it has little impact on the events' kinematic distributions. The first scan is performed at $M_A = 600$ GeV and $M_a = 250$ GeV, the second at $M_A = 700$ GeV $M_a = 350$ GeV. In both cases $\tan\beta = 1.0$.

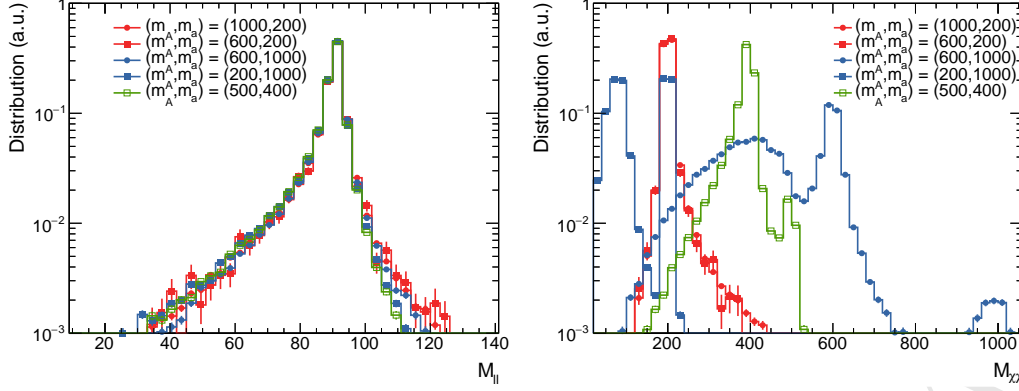


Figure 22: Distributions of the invariant mass of the dilepton (left) and $\chi\bar{\chi}$ systems (right) with no selection applied in addition to the generation cuts. The $M_{l\bar{l}}$ distribution is centered around the Z boson mass independent of the chosen parameter point, indicating that there is no contribution from γ^* exchange. The $M_{\chi\bar{\chi}}$ distribution

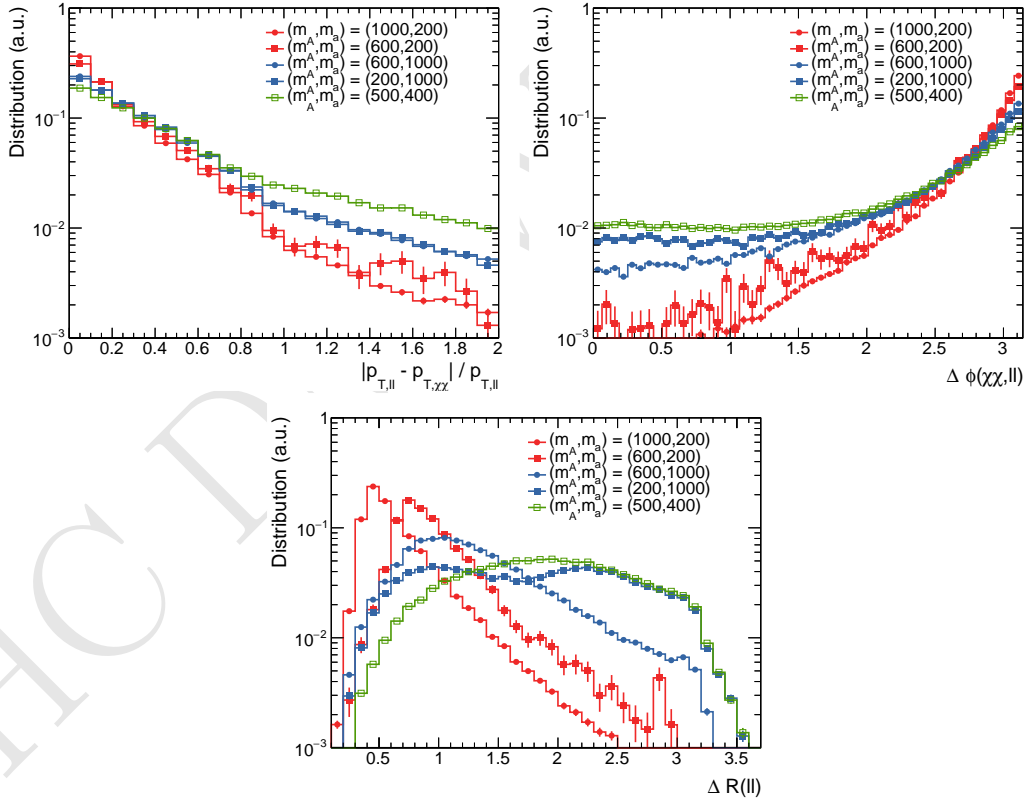


Figure 23: Distributions of the main selection variables after preselection: p_T balance (top panel), $\Delta\Phi$ (middle) and ΔR (bottom). The shown parameter points illustrate the different qualitative behavior in the three different mass regions.

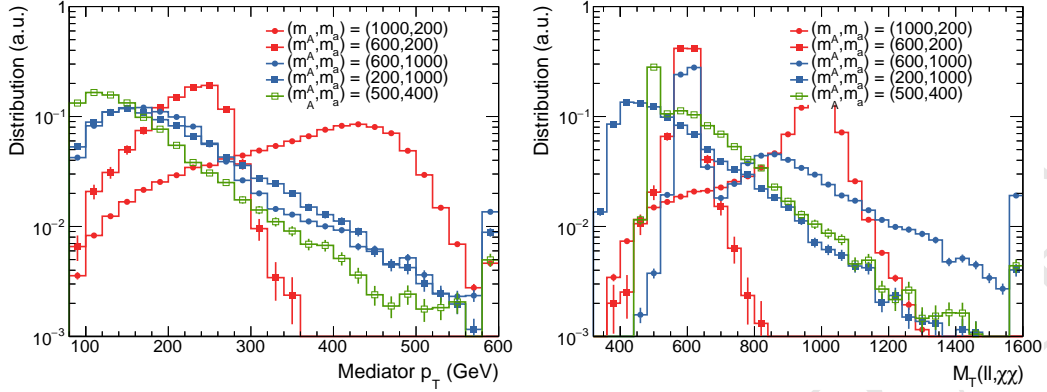


Figure 24: E_T^{miss} and MT distributions in the signal region. The E_T^{miss} distribution shows a Jacobian structure in the $M_A > M_a$ regime, the location of which strongly depends on M_A . In the region of inverted mass hierarchy $M_A < M_a$, the spectrum is less structured and does not fall off as steeply towards higher values. For a small mass splitting of $M_a - M_A \approx M_Z$, the spectrum is shifted to much lower values of E_T^{miss} . The MT distribution allows to access the resonant nature of the process. Clear mass peaks are present for the normal mass hierarchy. In the inverted region, the MT distribution is more sensitive to the mass difference $M_a - M_A$ than the E_T^{miss} distribution, allowing to differentiate between signal hypotheses that give near-identical E_T^{miss} distributions.

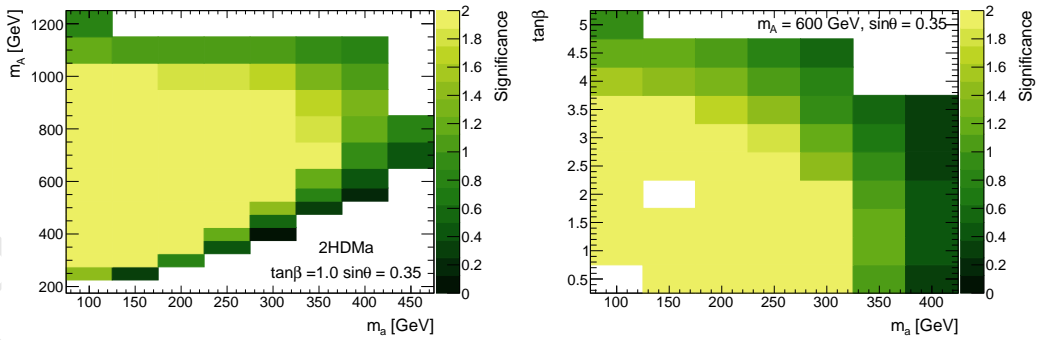


Figure 25: Expected significances are calculated using published background estimates and assuming a reconstruction efficiency of 75%. The LHC is expected to be sensitive to regions with significances greater than 2.

4.1.4 Studies of DM+heavy flavor signature

Heavy flavour final state have sizeable contributions to the production of the CP-even and CP-odd scalar mass eigenstates, due to the Yukawa structure of the couplings in the matter sector. In the following sections, the most important signatures involving either visible or invisible decays of the heavy Higgses are reviewed.

4.1.5 Recasting existing $tt+E_T^{\text{miss}}$ and $bb+E_T^{\text{miss}}$ signatures

These two signatures are dominantly produced in diagrams involving the invisible decays of the two CP-odd scalars. Their relevance is therefore determined by the two pseudoscalar masses, $m(A)$ and $m(a)$ and it is a function of $\sin\theta$ and $\tan\beta$. For both bb and tt associated productions, we find that the highest sensitivity of this signatures is obtained for high values of $\sin\theta$.

The 2HDM+a model is equivalent to a single pseudoscalar simplified model (DMF) when A is much heavier than a , and therefore the former does not contribute to the considered final state. However, when the two mediators are closer in mass, the $pp \rightarrow ttA$ contribution becomes more relevant as it is possible to observe in Figure 26, where the two models are compared assuming $m(A) = 750$ GeV and two different values for $m(a)$. An excellent agreement was observed between *DMSIMP* and *2HDMp* on parton-level variables sensitive to the helicity structure of the interaction between top and the mediator[?], if the invariant mass of the two DM particles in the 2HDM is required to be smaller than 200(300) GeV for $m(a) = 150(300)$ GeV respectively, giving confidence that, once the contribution from A production is separated, it is possible to fully map the $2HDM + a$ kinematics into the DMF simplified model.

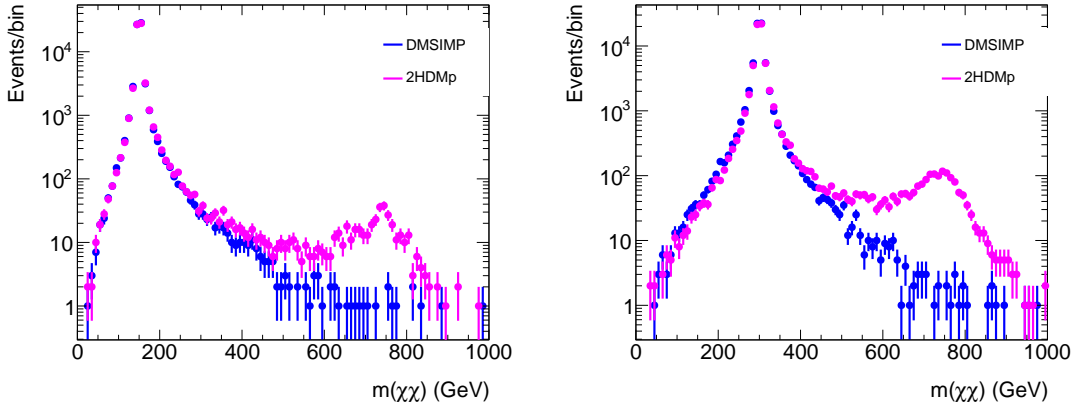


Figure 26: Comparison of $m(\chi\chi)$, the invariant mass of the two DM particles for the *DMSIMP* (blue) and the *2HDMp* model (magenta). The plot on the left (right) shows the comparison for $m(a) = 150(300)$ GeV respectively.

This remapping is achieved by taking for each set of the parameters the average of the selection acceptances for $m(A)$ and $M(A)$ as calculated with *DMSIMP* weighted by

the respective cross-section for A (σ_A) and a (σ_a) production, in formulas

$$Acc_{2HDM}(m(A), M(a)) = \frac{\sigma_a \times Acc_{DMSIMP}(m(a)) + \sigma_A \times Acc_{DMSIMP}(m(A))}{\sigma_a + \sigma_A} \quad (4.3)$$

The acceptance in this case is a parton level implementation of the two-lepton analysis described in [arXiv:1710.11412]. The acceptance estimated in this way is shown as red triangles in Figure 27, and an excellent agreement can be seen with the acceptances evaluated directly on the 2HDM samples. The acceptance estimated in this way is shown as red tri-

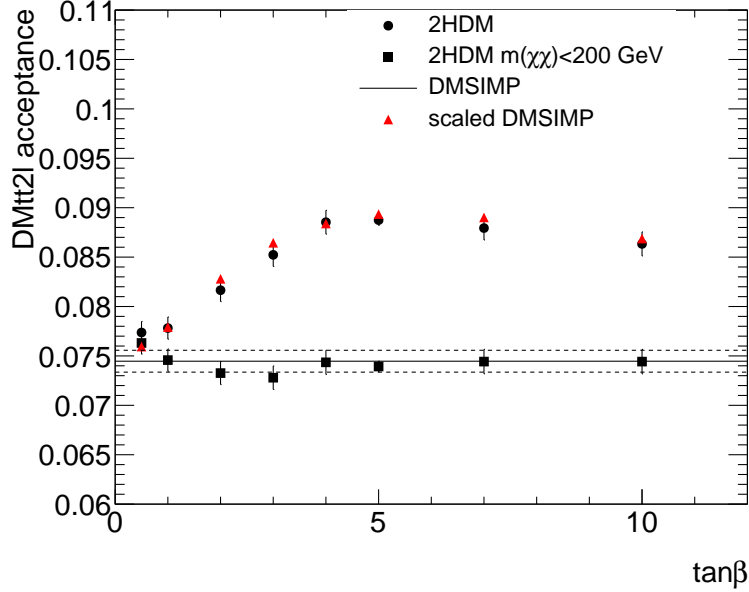


Figure 27: Acceptance of the two-lepton analysis as a function of $\tan \beta$ for the $2HDM_p$ model (round markers), for the $2HDM_p$ model considering only events with $m(\chi\chi) < 200$ GeV (square markers), and for the $DMSIMP$ model (full line) for a mediator mass of 150 GeV. The two dashed lines indicate the statistical error of the $DMSIMP$. The value of $m(A)$ is fixed at 600 GeV, and $\sin \theta = 0.35$. The acceptance calculated from the $DMSIMP$ acceptance rescaled following the prescription 4.3 (red triangles) is also shown.

angles in Figure 27, and an excellent agreement can be seen with the acceptances evaluated directly on the 2HDM samples. Further validation were performed also on the acceptances calculated for zero and one lepton final states [1710.11412,1711.11520], both as a function of $\sin \theta$ and $\tan \beta$ and can be observed in Fig 28. Finally, the formula was successfully tested also the situation in which $|m(A) - m(a)| \sim 50$ GeV, implying the possibility of a large interference between the production of the two bosons.

Motivations for an high $\tan \beta$ scan for $bb + E_T^{\text{miss}}$ The projection of sensitivity in $\tan \beta$ for benchmark #2, based on the CMS results for $bb + \text{MET}$ [arXiv:1706.02581] are shown in Figure 29. The reach for an upper bound on $\tan(\beta)$ with $bb + \text{MET}$ shows good potential, for $\tan \beta$ values above 10.

Say something about high width for H?

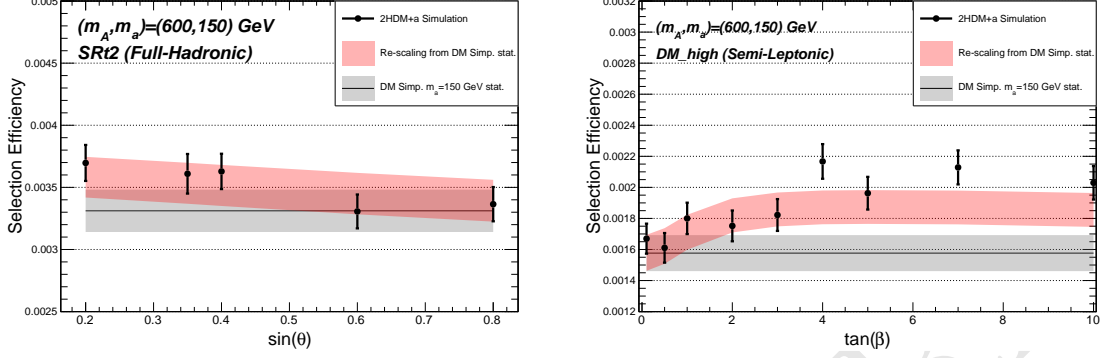


Figure 28: Validation of the re-scaling formula on zero and one lepton final states as a function of $\tan\beta$ and $\sin\theta$ parameters

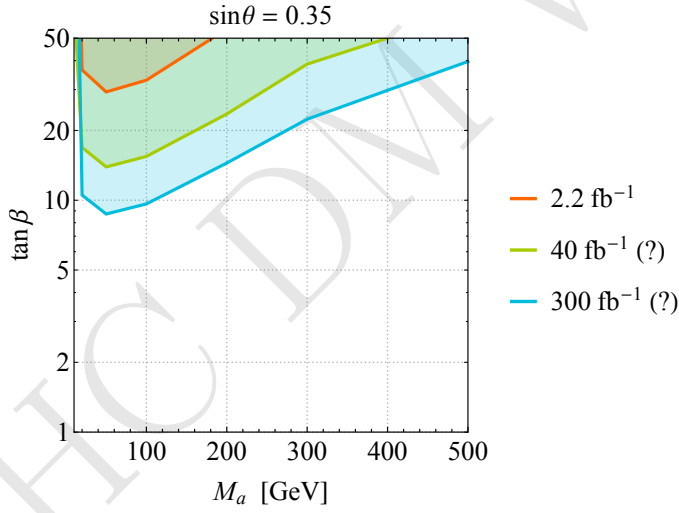


Figure 29: Sensitivity projection for benchmark #2 based on the CMS results for $bb+\text{MET}$ [arXiv:1706.02581].

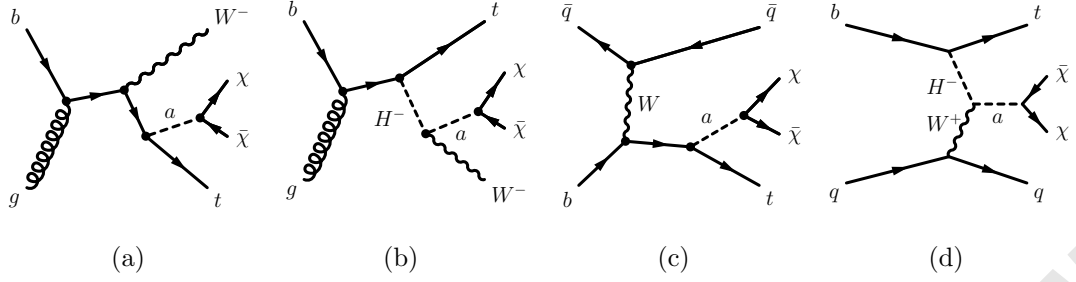


Figure 30: Representative diagrams for tW and t -channel production of DM in association with a single top quark.

4.1.6 Motivation for a dedicated $tW + E_T^{\text{miss}}$ search

The sensitivity of the LHC experiments to the associated production of dark matter with a single top has been recently studied [?] in the framework of an extension of the standard model featuring two Higgs doublets and an additional pseudoscalar mediator. This study extends the work of previous literature [?], which demonstrated using a simplified model that the consideration of final states involving a single top quark and DM (DMt) increases the coverage of existing analyses targeting the $DMt\bar{t}$ process.

Like single top production within the SM, the DMt signature in the model receives three different types of contributions at leading order (LO) in QCD. These are t -channel production, s -channel production and associated production together with a W boson (tW) (Fig. 30). When the decay $H^\pm \rightarrow W^\pm a$ is possible, the H^\pm is produced on-shell, and the cross-section of $pp \rightarrow tW\chi\chi$, assuming H^\pm masses of a few hundred GeV, is around one order of magnitude larger than the one for the same process in the simplified model. Moreover the production and cascade decay of a resonance yields kinematic signatures which can be exploited to separate the signal from the SM background.

Dedicated selections considering one and two lepton final states are developed to assess the coverage in parameter space for this signature at a centre-of-mass energy of 14 TeV assuming an integrated luminosity of 300 fb^{-1} in Ref. [?]. Background and signal Monte Carlo simulated samples are employed for the estimate of the results. The effect of the detector on the kinematic quantities utilised in the analysis is simulated by applying a Gaussian smearing to the momenta of the different reconstructed objects and reconstruction and tagging efficiency factors. Figure 31 shows the sensitivity reach for two of the parameter scans proposed in this whitepaper. On the top panel the exclusion reach for the $m(a), \tan\beta$ plane is presented, assuming $\sin\theta = 0.35$ and $m(A) = m(H^\pm) = m(H) = 500 \text{ GeV}$. It is possible to observe that for this scenario the sensitivity reach is comparable to the one from the mono-h signature as presented in Ref. [?]. On the bottom panel of Figure 31 the signature's sensitivity to benchmark #4 is evaluated for the first time.

4.1.7 Uncovered signatures with $tth + E_T^{\text{miss}}$

As discussed in Section ??, the production of the heavy mediator A gives a sizeable contribution to the $t\bar{t} + E_T^{\text{miss}}$ production cross section in the $2HDM + a$ model. This is also

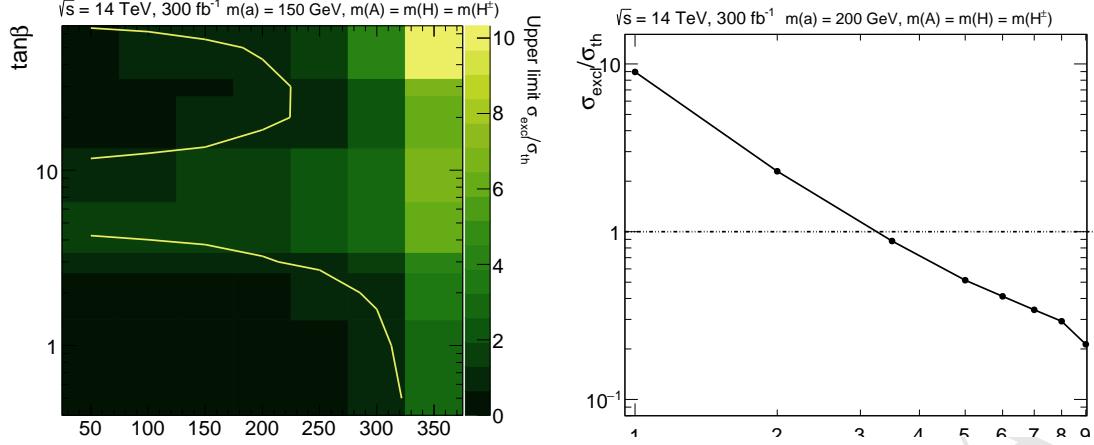


Figure 31: Exclusion reach for benchmark #2 (top) and benchmark #4 (bottom), assuming $\sin\theta = 0.35$ and $m(A) = m(H^\pm) = m(H) = 500$ GeV.

true for the heavy H . When the decay of these mediators into the lightest pseudoscalar a is allowed, this decay process dominates over the direct decay into $\chi\chi$. In symmetry with what happens for the mono-h signature discussed in [?], for certain region of parameter space the signatures $pp \rightarrow t\bar{t}A \rightarrow t\bar{t}ah$ and $pp \rightarrow t\bar{t}H \rightarrow t\bar{t}aZ$ become sizeable. For the former case, it can be estimated from Fig. 12(b) of Ref. [?] that for relatively small $m(A)$ the $pp \rightarrow t\bar{t}ah$ cross section can be up to 30% that of the $pp \rightarrow t\bar{t}\chi\chi$ process. The interplay between the parameters of the model, and especially between the heavy higgs masses for these types of final state render the phenomenology interesting and variegated, as can be seen for example in the branching ratio study of Fig. 32, although further studies are needed to fully understand the interplay and the complementarity between these $t\bar{t}h + E_T^{\text{miss}}$ channels and the traditional heavy flavour dark matter searches.

4.1.8 Top pair resonant searches

Heavy scalar and pseudoscalar bosons decaying dominantly into top-quark pairs can be searched for by studying the resulting $t\bar{t}$ invariant mass spectra. However, interference effects between the signal processes and the SM $t\bar{t}$ production distort the signal shape from a single peak to a peak-dip structure [appropriate REFs?]. Interference between a loop-induced and a tree-level process cannot currently be simulated in MadGraph. To amend this problem, the "Higgs_Effective_Couplings_FormFactor" approach [?] is implemented in the UFO, replacing the loop production by an effective vertex. **Are we interested to insert one of the validation plots from atlas?**

4.1.9 Four tops final states

Work in progress

4.1.10 Final proposal for parameter scan

- a two-dimensional scan in the light pseudoscalar mass (m_a) - heavy pseudoscalar mass (m_A) plane where $m_a = m_A$, fixing $\tan\beta$ to 1.0, $\sin\theta$ to 0.35 and the

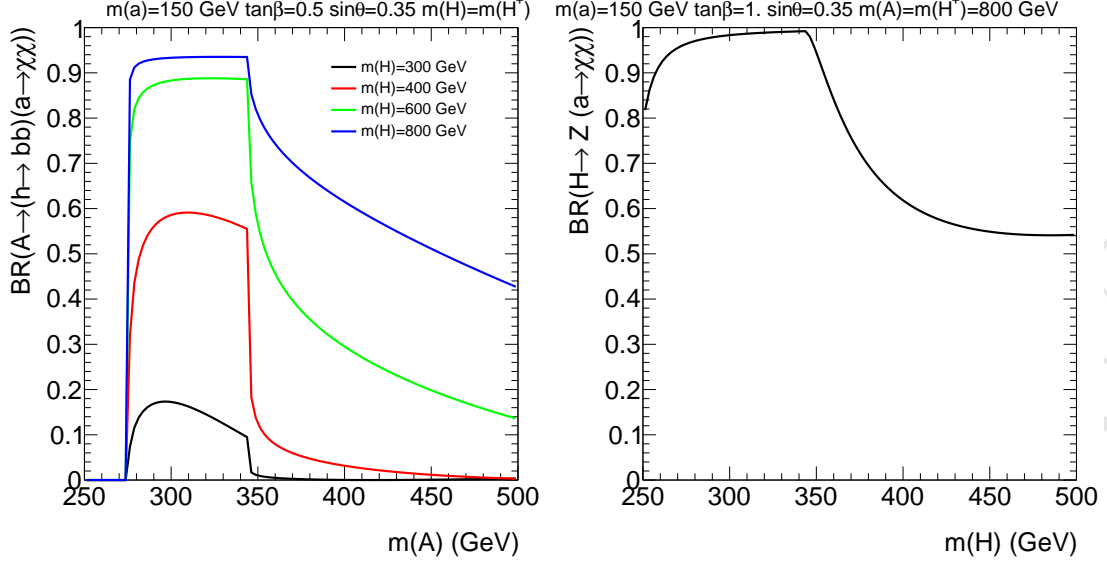


Figure 32: Example of the dependence of the A and H branching ratio into ah as a function of some parameters of the 2HDM model.

Dark Matter mass (m_{DM}) to 10 GeV.

- a one-dimensional scan in DM mass from 1 GeV to 500 GeV for a point in the middle of the sensitivity range for the mono- V analyses at $m_A=600$, $m_a=250$ GeV, so the connection between this model and cosmology is clear as the measured relic density starts being satisfied at values of DM mass around 100 GeV

In order to explore changes in complementarity with different analyses and kinematics, this should be complemented by:

- a two-dimensional scan in the m_a - $\tan\beta$ plane, for comparison with the $t\bar{t} + \text{MET}$ / $b\bar{b} + \text{MET}$ analyses. In this case, the charged Higgs mass (m_{H^\pm}), the heavy pseudoscalar mass (m_A) and the heavy Higgs mass (m_H) should be fixed to 600 GeV. This scan includes points: 50, 45, 40, 35, 30, 25, 20, 15, 10, 5 for $M(a)$ masses between 10 and 350 GeV. The high- $\tan\beta$ points would be of primary interest to the HF + DM searches. Uli's studies have shown that one can simply reweight the existing $t\bar{t} + \text{DM}/b\bar{b} + \text{DM}$ models from DMF to the new 2HDM+PS cross sections; full simulation of the newly proposed 2HDM+PS points is not required.
- two one-dimensional scans in $\sin\theta$ for the comparison of mono-Higgs and $b\bar{b} + \text{MET}$ analysis (it is expected that the $b\bar{b} + \text{MET}$ analysis will only have to rescale previous models/cross-sections) [2]: - $m_H = m_A = m_{H^\pm} = 600\text{GeV}$, $m_a = 200\text{GeV}$, $\tan\beta=1$
- $m_H = m_A = m_{H^\pm} = 1000\text{GeV}$, $m_a = 350\text{GeV}$, $\tan\beta=1$

The PDF recommended is five-flavor. ATLAS will use the NNPDF3.0 PDF set. Some text by Fabio Maltoni and Ulrich Haisch can be found in the `texinputs_app` folder.

5 Connection with cosmology

5.1 TODO

- **General**

Polish text.

Need very clear statements about what parameters are used. This will probably already be described elsewhere.

- **2D M_χ - M_A scan**

Done.

- **1D M_χ scan**

Beautify plot.

Add description in text

- **Add other scans?**

5.2 Actual content

An important requirement for models of dark matter is their consistency with existing astrophysical observations, namely the observed dark matter relic density. The relic density is driven by the annihilation cross-section of dark matter into SM particles. For a given model of dark matter-SM interactions, the annihilation cross-section is fully defined and a calculation of the resulting relic density can be performed.

We use the MADDM [? ?] plugin for MG5_aMC@NLO in order to calculate the present-day relic density for this model. By modeling the thermal evolution of the cross-section during the expansion of the early universe, the time of freeze-out is determined. All tree-level annihilation processes are taken into account, and the Yukawa couplings of all fermions are taken to be non-zero. The Feynman diagrams of annihilation processes taken into account in this calculation are shown in fig. ?? . Generally, the annihilation proceeds via single or double s-channel exchange of the pseudoscalars a and A , with subsequent decays. Since MADDM uses only tree-level diagrams, contributions from off-shell pseudoscalars can only be taken into account for the case of single s-channel mediation with direct decay of the pseudoscalar to SM fermions. If the pseudoscalar instead decays to other bosons or if the annihilation proceeds through double s-channel diagrams, the outgoing bosons are taken to be on-shell and their decays are not simulated.

The relic density is shown for a scan in the M_a - M_χ plane in fig. ?? . For small values of M_χ below the mass of the top quark, DM is mostly overabundant. In this regime, annihilation to quarks is suppressed by the small Yukawa couplings of the light fermions. The observed relic density can only be achieved for $M_\chi \approx M_a/2$, where annihilation is resonantly enhanced, or for $M_\chi \approx (M_a + M_h)/2$, close to the threshold for the $\chi\chi \rightarrow ha$ process. Above the top threshold, annihilation into fermions becomes very efficient and DM is underabundant. As M_χ increases further, annihilation via single s-channel

diagrams is increasingly suppressed and the relic density rises again. The observed density is reproduced again for $M_\chi \approx 1\text{TeV}$ at low M_a .

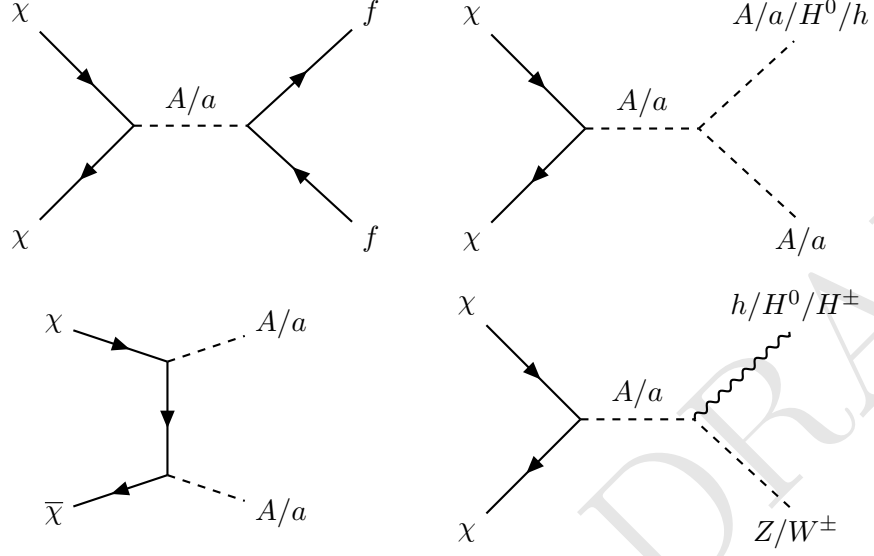


Figure 33: Annihilation diagrams taken into account in the relic density calculation.

6 Conclusions

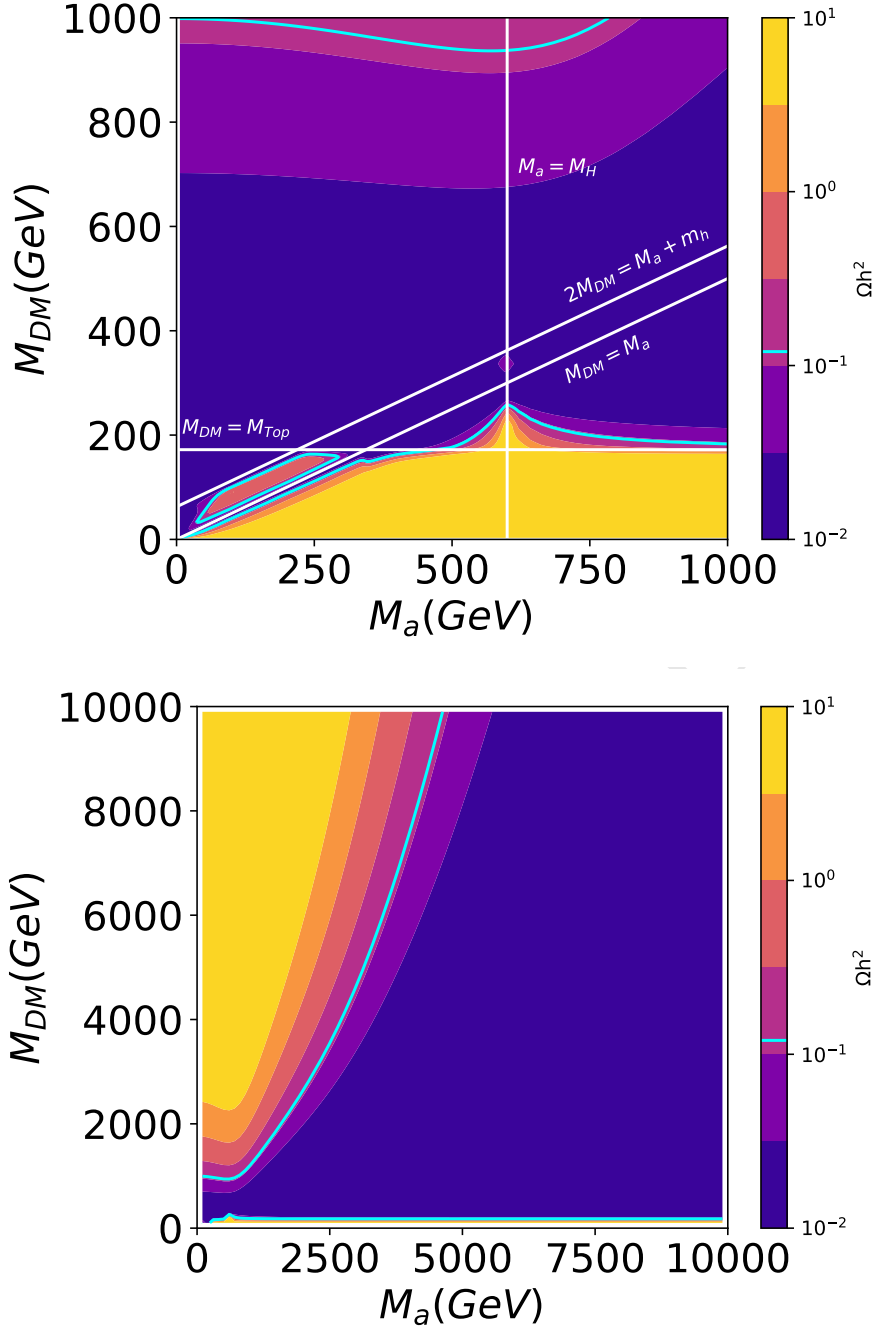


Figure 34: Predicted relic density for a two-dimensional scan of M_χ and M_a . The color scale indicates the relic density, the cyan solid line shows the observed value of $\Omega h^2 = 0.12$. The color scale is truncated at its ends, i.e. values larger than the maximum or smaller than the minimum are shown in the same color as the minimum / maximum. While the top panel focuses on the mass region relevant to collider searches, the bottom panel shows the development of the relic density for a larger mass region.

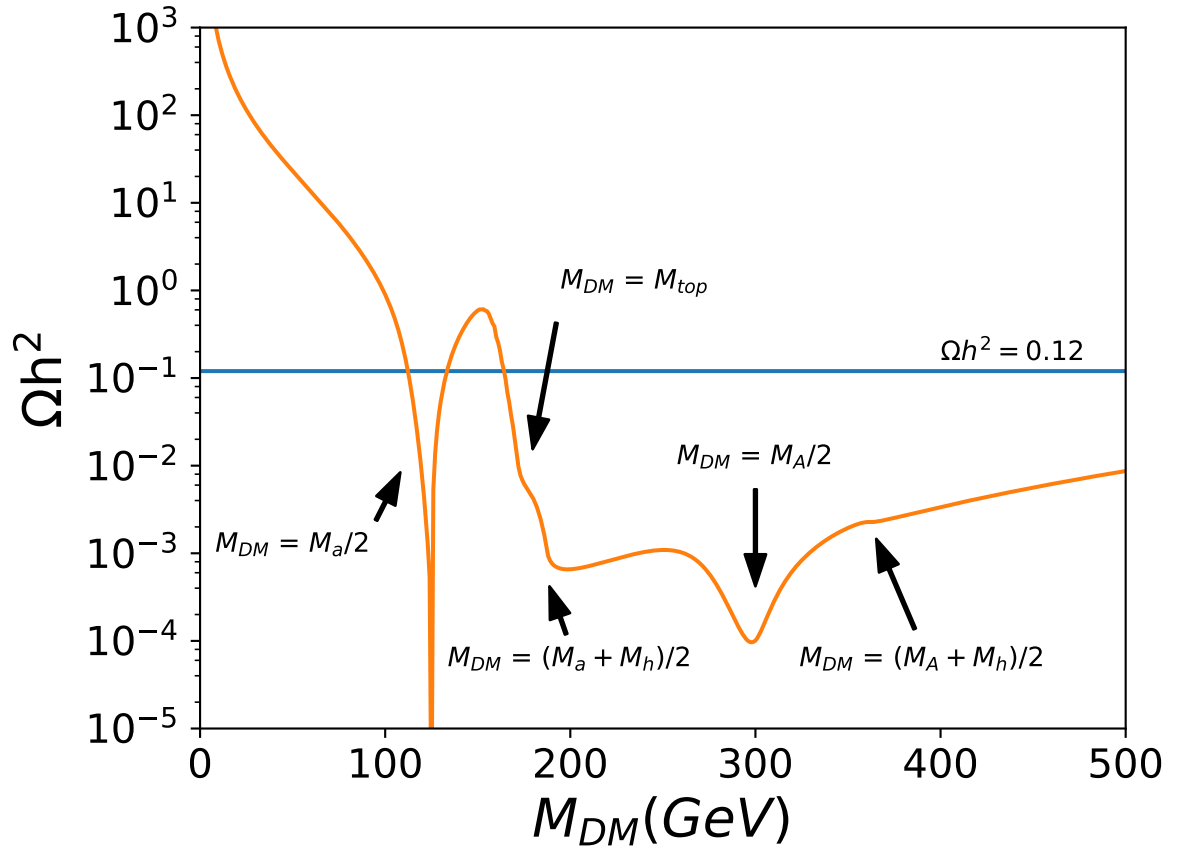


Figure 35: Relic density for a one-dimensional scan of M_χ .